

Prospects of non-resonant di-Higgs searches and Higgs boson self-coupling measurement at the HE-LHC using machine learning techniques

Amit Adhikary^a Rahool Kumar Barman^b Biplob Bhattacharjee^a

^aCentre for High Energy Physics, Indian Institute of Science, Bangalore 560012, India

^bSchool of Physical Sciences, Indian Association for the Cultivation of Sciences, Kolkata, 700040, India

E-mail: amitadhikary@iisc.ac.in, psrkb2284@iacs.res.in,
biplob@iisc.ac.in

ABSTRACT: The prospects of observing the non-resonant di-Higgs production in the Standard Model at the proposed high energy upgrade of the LHC, *viz.* the HE-LHC ($\sqrt{s} = 27$ TeV and $\mathcal{L} = 15$ ab⁻¹) is studied. Various di-Higgs final states are considered based on their cleanliness and signal yields. The search for the non-resonant double Higgs production at the HE-LHC is performed in the $b\bar{b}\gamma\gamma$, $b\bar{b}\tau^+\tau^-$, $b\bar{b}WW^*$, $WW^*\gamma\gamma$, $b\bar{b}ZZ^*$ and $b\bar{b}\mu^+\mu^-$ channels. The signal-background discrimination is performed through multivariate analyses using the Boosted Decision Tree Decorrelated (BDTD) algorithm in the TMVA framework, the XGBoost toolkit and Deep Neural Network (DNN). The variation in the kinematics of Higgs pair production as a function of the self-coupling of the Higgs boson, λ_h , is also studied. The ramifications of varying λ_h on the $b\bar{b}\gamma\gamma$, $b\bar{b}\tau^+\tau^-$ and $b\bar{b}WW^*$ search analyses optimized for the SM hypothesis is also explored.

Contents

1	Introduction	1
2	Non-resonant di-Higgs production at the HE-LHC	5
2.1	The $b\bar{b}\gamma\gamma$ channel	6
2.2	The $b\bar{b}\tau\tau$ channel	11
2.3	The $b\bar{b}WW^*$ channel	15
2.4	The $WW^*\gamma\gamma$ channel	19
2.5	The $b\bar{b}ZZ^*$ channel	21
2.5.1	The $2b4l'$ channel	23
2.5.2	The $2b2e2\mu$ channel	25
2.6	The $b\bar{b}\mu\mu$ channel	28
3	Higgs self-coupling measurement	30
4	Summary	35
A	Outlining the generation cuts and production cross sections for the signal and backgrounds	47

1 Introduction

The discovery of the Higgs boson in 2012, by the ATLAS [1] and CMS [2] collaborations, laid the foundation stone to a new era in the field of particle physics. Since its discovery, numerous measurements have been performed to unravel the properties of the observed 125 GeV resonance, and these results indicate towards its compatibility with the properties of the Higgs boson as predicted by the Standard Model (SM) of particle physics. The couplings of the observed Higgs boson with the third generation quarks and leptons, and the gauge bosons, fall within the allowed SM uncertainties and have been measured with considerable precision [3–10]. However, we still have a long way to go along the precision frontier in the measurement of the first and second generation Yukawa couplings. Another important aspect of the the Standard Model which has remained elusive till now is the

Higgs potential. The location of the minimum of the Higgs potential has been successfully measured, however, we are yet to observe any clear signature of the self-coupling of the Higgs boson (λ_h) which is another key ingredient in the understanding of the stability of the Higgs potential.

In the SM, the only direct probe to measure λ_h is the non-resonant pair production of the Higgs bosons. The difficulty in its measurement emerges from the smallness of the di-Higgs production cross-section. At the leading order (LO), the Feynman diagrams which dominantly contribute to the non-resonant Higgs pair production process proceeds through top quark loops in the gluon fusion channel with a destructive interference between the triangle and the box diagrams. The fine cancellation results in a smaller production cross-section. At the centre of mass energy (\sqrt{s}) of 13 TeV, the SM di-Higgs production cross-section in the gluon fusion channel stands at $31.05^{+2.2\%}_{-5.0\%}$ fb at the NNLO level [11], while the production rate at $\sqrt{s} = 14$ TeV increases to only $36.69^{+2.1\%}_{-4.9\%}$ fb [11] at the NNLO level. The cross-section of di-Higgs production through other modes namely vector boson fusion, associated production with vector bosons and associated production with top and bottom pairs are much smaller than the production rate in the gluon fusion channel, and, are generally ignored. The small signal production rate is however compensated by the presence of two Higgs bosons which can give rise to phenomenologically rich final states.

Various beyond the SM (BSM) scenarios can also enhance the di-Higgs production cross-section. New physics (NP) cases, such as the presence of an extended Higgs sector with a heavier resonance which can decay into a pair of SM-like Higgs bosons, composite Higgs models, strongly interacting theories, effective field theories (EFT) with modified top Yukawa coupling, Supersymmetric and extra-dimension theories with heavy colored states, can potentially increase the di-Higgs production cross-section. A wide array of studies pertaining to the case of di-Higgs production in various NP models can be found in Refs. [12–72].

The ATLAS and CMS collaborations have also performed numerous searches in various non-resonant di-Higgs final states using both Run-I and the Run-II dataset. While none of these searches have reported any excess over the SM background, upper limits have been derived on the di-Higgs production cross-section. The most stringent upper limit has been derived by ATLAS [73] through a combination of searches in the $4b$, $b\bar{b}WW^*$, $b\bar{b}\tau^+\tau^-$, $4W$, $b\bar{b}\gamma\gamma$ and the $WW^*\gamma\gamma$ channels using the Run-II data collected at an integrated luminosity (\mathcal{L}) of $\sim 36 \text{ fb}^{-1}$. The upper limit stands at 6.9 times the SM production cross-section and the Higgs self-coupling is constrained within $-5.0 < k_\lambda < 12.0$ (where, k_λ is the ratio of λ_h over the SM value of Higgs self-coupling), at 95% confidence level (CL). The same dataset has also been used by ATLAS and CMS to perform non-resonant di-Higgs searches in the $4W$ [74], $b\bar{b}WW^*$ [75], $b\bar{b}\tau^+\tau^-$ [76, 77], $WW^*\gamma\gamma$ [78], $b\bar{b}\gamma\gamma$ [79, 80] and the $4b$ [81] final states. Among these results, searches in the $b\bar{b}\tau^+\tau^-$ [76], $4b$ [81] and

the $b\bar{b}\gamma\gamma$ [79] channels yield an upper limit of 12.7, 22 and 13 times the SM cross-section value at $\sqrt{s} = 13$ TeV, respectively, at 95% CL, while the other channels result in much weaker upper limits. Similarly, the analogous searches by CMS in the $b\bar{b}\gamma\gamma$ [80] and the $b\bar{b}\tau^+\tau^-$ [77] channels have reported an upper limit of 19.2 and 30 times the SM di-Higgs production cross-section, respectively, at 95% CL. Searches have also been performed in the $b\bar{b}l\nu l\nu$ final state by both ATLAS and CMS using the LHC Run-II data collected at $\sim 139 \text{ fb}^{-1}$ and $\sim 36 \text{ fb}^{-1}$, respectively, and the corresponding upper limits at 95% CL stand at 40 [82] and 79 [83] times the SM production cross-section, respectively. CMS has also combined the search results from $b\bar{b}\tau^+\tau^-$, $b\bar{b}\gamma\gamma$, $4b$ and the $b\bar{b}VV$ ($V = W^\pm, Z$) channels and derived an upper limit at 22.2 times the SM non-resonant di-Higgs production cross-section at 95% CL [84]. The non-resonant di-Higgs searches performed by ATLAS and CMS using Run-I dataset and the Run-II dataset collected at $\mathcal{L} \sim 2 \text{ fb}^{-1}$ can be found in Refs. [85–89]. Indirect measurement of λ_h has also been performed by ATLAS using the LHC Run-II dataset ($\mathcal{L} \sim 80 \text{ fb}^{-1}$) [90] and has excluded k_λ outside $-3.2 < k_\lambda < 11.9$ at 95% CL. The indirect probe makes use of single Higgs production at next-to-leading order (NLO) where the electroweak loop corrections are sensitive to the self-coupling of the Higgs boson. In Ref. [91], a combination of indirect searches through single Higgs production using Run-II data collected at $\mathcal{L} \sim 80 \text{ fb}^{-1}$ and non-resonant di-Higgs searches in the $4b$, $b\bar{b}\tau^+\tau^-$ and $b\bar{b}\gamma\gamma$ channels using Run-II data collected at $\mathcal{L} \sim 36 \text{ fb}^{-1}$, results in the allowed range of k_λ to be within $[-2.3 : 10.3]$ at 95% CL. The potential reach of the high luminosity upgrade of the LHC (HL-LHC: $\sqrt{s} = 14$ TeV, $\mathcal{L} \sim 3000 \text{ fb}^{-1}$) in probing k_λ has also been studied by ATLAS in the $b\bar{b}\gamma\gamma$ search channel [92]. This search reports a signal significance of 1.05σ and a projected exclusion region of $-0.8 \leq k_\lambda \leq 7.7$ at 95% CL. Through a combination of searches in the $4b$, $b\bar{b}\gamma\gamma$ and the $b\bar{b}\tau^+\tau^-$ channels, ATLAS has reported a projected signal significance of 3.5σ [93].

Numerous phenomenological studies have also focused on exploring the future prospects of non-resonant di-Higgs searches and λ_h measurement at the HL-LHC, and, have exhibited encouraging results through the use of novel kinematic variables, variables constructed from boosted objects, jet substructure techniques, precision calculations and multivariate analysis techniques [94–106]. In addition, the prospects of measuring λ_h in the future lepton colliders has also been studied (see Refs. [107–109]). Indirect measurements of λ_h at the HL-LHC and the future lepton colliders have also been performed through the study of single Higgs boson production (see Refs. [29, 110–116]). The electroweak oblique parameters have also been used to probe λ_h in Ref. [117]. The complementarity between the direct and indirect measurements of λ_h offer an interesting avenue for advancement of our understanding about the Higgs potential, however, we must note that the indirect probes would be more vulnerable to the NP couplings present in the loop corrections and offers a higher degree of complicity in extracting model-independent limits. Therefore, the direct probe of λ_h offers more viable options for model-independent studies. However, we must also note

that the numerous direct searches of λ_h performed in the context of the HL-LHC point towards a common conclusion that the future prospect of observing the non-resonant di-Higgs signal is rather bleak unless new physics effects are present or the signal-background discrimination efficiency of the analysis techniques improves considerably. We would also like to point out that an extensive list of studies exist in the literature where the potential capability of the ambitiously proposed $\sqrt{s} = 100$ TeV hadron collider in probing λ_h has been explored [99, 106, 118–124]. The future prospects of di-Higgs searches at the 100 TeV hadron collider have also been studied in the context of Higgs portal models and in the Higgs EFT framework in Refs. [26, 32, 49, 125–127]. On the contrary, much less impetus has been given towards studying the potential reach of the more realizable proposed energy upgrade to the HL-LHC, *viz.* the HE-LHC which is projected to reach $\sqrt{s} = 27$ TeV at an integrated luminosity of $\mathcal{L} \sim 15 \text{ ab}^{-1}$, in constraining λ_h , and the corresponding exhaustive studies are by and large missing from literature. This stimulates the necessity for a comprehensive study of the future potential of the HE-LHC.

In this work, we perform a systematic evaluation of various final states emerging from non-resonant di-Higgs production at the HE-LHC, with inclusion of an exhaustive list of backgrounds, assessment of detector effects and implementation of advanced multivariate analysis techniques. Before giving a detailed outline of this paper, we briefly revisit the existing works where the potential capability of the HE-LHC in probing the Higgs boson self-coupling has been studied. The SM non-resonant di-Higgs production cross-section at $\sqrt{s} = 27$ TeV in the gluon fusion channel is $139.9^{+1.3\%}_{-3.9\%} \text{ fb}$ at NNLO [11] and is roughly ~ 3.5 times larger than its 14 TeV counterpart. In the context of HE-LHC, the $b\bar{b}\gamma\gamma$ channel has been studied in detail in Refs. [122, 128, 129]. Ref. [122] reports a 5σ observation at the HE-LHC for $\mathcal{L} \sim 2.5 \text{ ab}^{-1}$ and a potential measurement accuracy of 15% and 30% at 68% and 95% CL, respectively. Ref. [129] also reports a 5σ observation and a projected exclusion reach of $0.2 < k_\lambda < 1.8$ at 95% CL. A summary of the indirect probes of λ_h through single Higgs production and differential distribution measurements can also be found in Ref. [129]. Lastly, Ref. [128] outlines a $\geq 4.5\sigma$ observation at $\sim 40\%$ measurement accuracy for $\mathcal{L} \sim 15 \text{ ab}^{-1}$. The potential reach of other di-Higgs search channels have, however, remained largely unexplored. Furthermore, the combination of search results from multiple final states was observed to yield the most stringent constraints on λ_h for the case of LHC Run-I and Run-II measurements, as well as the HL-LHC projections, and we aim to explore this facet for the HE-LHC in the present study.

In the first part of our analysis, we study the $b\bar{b}\gamma\gamma$, $b\bar{b}\tau^+\tau^-$, $b\bar{b}WW^*$, $WW^*\gamma\gamma$, $b\bar{b}ZZ^*$ and the $b\bar{b}\mu^+\mu^-$ final states emerging from the decay of the Higgs pair. The choice of these final states is motivated either by the cleanliness with respect to the backgrounds and/or larger branching ratio of the decay modes of the Higgs boson along with non-availability of existing studies. Previous studies have indicated the effectiveness of multivariate analysis

in performing signal-background discrimination, and at times have exhibited an enhanced efficiency in improving the statistical signal significance compared to the more traditional cut-based analysis techniques [98–101, 130]. Consequently, we adhere to multivariate analysis in this work, and choose a variety of kinematic variables in each of the aforesaid analysis channels chosen through a wide literature survey. Our main goal is to improve the signal significance. In our study, we have considered three different multivariate analysis techniques. The first one is based on the Boosted Decision Tree Decorrelated (BDTD) algorithm in the TMVA framework [131], in the second case, we use the XGBoost [132] toolkit which utilizes a gradient tree boosting algorithm, and thirdly, we use Deep Neural Network (DNN) [133–135].

The objective of this work can be broadly classified into two different sections: to estimate the discovery reach of non-resonant di-Higgs searches at the HE-LHC through multivariate analysis using the BDTD algorithm, the XGBoost toolkit, and the DNN framework in various well-motivated di-Higgs final states (Sec. 2) and assess HE-LHC’s future potential in constraining λ_h (Sec. 3). We also study the ramifications of varying λ_h on the di-Higgs signal sensitivity in Sec. 3. We conclude in Sec. 4.

2 Non-resonant di-Higgs production at the HE-LHC

In this analysis, we consider such di-Higgs final states which have photons and/or leptons in the final state, *viz.* $b\bar{b}\gamma\gamma$, $b\bar{b}\tau^+\tau^-$, $b\bar{b}WW^*$, $WW^*\gamma\gamma$, $b\bar{b}ZZ^*$ and $b\bar{b}\mu^+\mu^-$. Final states like $\tau^+\tau^-WW^*$, $\tau^+\tau^-ZZ^*$, 4τ , $ZZ^*\gamma\gamma$, 4γ , $4Z$ and $4W$ have not been considered due to negligible production rates at the HE-LHC. However, it must be noted that some of these channels might have crucial implications on di-Higgs searches at the 100 TeV collider.

The di-Higgs signal and the background events have been generated at the leading order (LO) parton level with MG5_aMC@NLO [136]. The NNPDF2.3LO PDF set [137] has been used with the A14 tune [138]. The showering and hadronization has been done with Pythia8 [139]. Fast detector response has been simulated using Delphes-3.4.1 [140]. Since the detector configuration at the HE-LHC is not known, we simulate the detector effects by assuming the resolution and tagging efficiencies of the present ATLAS detector.

The *jet* reconstruction is been done using the anti- kT [141] algorithm with jet radius parameter, $R = 0.4$, and the minimum jet transverse momentum, $p_T^j > 20$ GeV, in the FastJet [142] framework. For the leptons (l , $l = e, \mu$) and photons to be isolated, it is required that the sum of transverse momenta of the surrounding objects within a cone of radius $\Delta R = 0.2$ must be less than 20% of the p_T of the lepton or photon under consideration. Furthermore, the leptons and photons are also required to lie within a pseudorapidity range of $|\eta| \leq 4.0$ and must carry $p_T > 5$ GeV and > 10 GeV, respectively. A flat b -tagging efficiency of 70% has been considered while the $c \rightarrow b$ and $j \rightarrow b$ fake rates have been fixed

at 3% (4%) and 0.15% (0.12%) provided the transverse momentum (p_T) of the c and j are in between 30 – 90 GeV (> 90 GeV), respectively [143]. We must mention that the fake rates are a function of the transverse momenta and pseudorapidity (η), and must be dealt with more sophistication in a more precise analysis.

We perform a multivariate analysis in the TMVA framework to efficiently discriminate the signal and the background events. In this respect, multifarious kinematic variables are chosen depending upon the di-Higgs final state. We use the BDTD algorithm in all these analyses. Overtraining of the signal and background samples has been avoided by requiring the results of the Kolmogorov-Smirnov test to be always > 0.1 . We also perform a detailed collider analysis using the XGBoost package and DNN. The XGBoost training is performed by optimizing the learning rate, max-depth, and the regularization parameters, η and λ . We also use early stopping for regularization. The goal is to minimize the loss function and avoid overtraining by maintaining a comparable validation loss and training loss. The XGBoost classifier is trained with the signal and background event samples, and a lower cut is applied on the signal-like probability of the XGBoost output. We refer to this lower limit as the probability cut on the XGBoost output. We also use a DNN classifier to train the signal and the background events. The DNN training is performed on a three-layered network structure with Adam optimizer, and regularization is performed using batch normalization. The categorical cross-entropy loss function is considered, and similar to the case of XGBoost, the aim is to minimize the loss function while maintaining a similar training loss and validation loss to avoid overtraining.

In the following subsections, we discuss the kinematic features of the numerous di-Higgs final states, provide a detailed outline of the analysis strategies and present our results from the detailed collider search. We begin our discussion by studying the features and prospects of the $b\bar{b}\gamma\gamma$ channel (which is one of the most promising channels for non-resonant di-Higgs searches at the HL-LHC) in the context of searches at the HE-LHC.

2.1 The $b\bar{b}\gamma\gamma$ channel

The small branching ratio of $h \rightarrow \gamma\gamma$ puts the signal ($pp \rightarrow hh \rightarrow b\bar{b}\gamma\gamma$) production rate at a downside, however, the relatively low production rate is compensated by the cleanliness of this channel. Numerous previous works have studied the prospects of this search channel in probing non-resonant di-Higgs production at the HL-LHC. In our previous work [101], where the HL-LHC prospects of the $b\bar{b}\gamma\gamma$ search channel was analyzed through both, cut-based and multivariate techniques, we had obtained a signal significance of ~ 1.46 and ~ 1.76 , respectively, thus, exhibiting a promising prospect for the high energy upgrade of the HL-LHC, *viz.* the HE-LHC.

The QCD-QED $b\bar{b}\gamma\gamma$ process is the most dominant source of background and has been generated upon merging with an additional *jet* through the MLM merging scheme [144].

Acceptance cuts
$N_{b \text{ jets}} = 2, N_{\gamma} = 2$
$122 \text{ GeV} < m_{\gamma\gamma} < 128 \text{ GeV}$
$\Delta R_{b\gamma} > 0.2$
$m_{bb} > 50 \text{ GeV}$

Table 1: Acceptance cuts for the multivariate BDTD analysis in the $b\bar{b}\gamma\gamma$ channel.

Substantial contribution to the background also arises from the fakes, *viz.* the $c\bar{c}\gamma\gamma$ and $j\bar{j}\gamma\gamma$ processes, when the c jets and the light jets (j), respectively, gets faked as a b jet. These three background processes ($b\bar{b}\gamma\gamma + c\bar{c}\gamma\gamma + j\bar{j}\gamma\gamma$) will be collectively referred to as $b\bar{b}\gamma\gamma^*$ in the remainder of this analysis. Other fake backgrounds which can contaminate the signal are: $b\bar{b}j\gamma$ and $c\bar{c}j\gamma$ (collectively referred to as Fake 1), and, $b\bar{b}jj$ (referred to as Fake 2). In the Fake 1 category, one light jet gets faked as a photon while two light jets are required to get misidentified as photons in the Fake 2 category. Another source of fake background is the hjj^* process ($hjj + hcc$) when h decays into photon pair and the j/c gets faked as a b jet. The other processes which contribute to the background are $t\bar{t}h$, Zh , $b\bar{b}h$ and $Z\gamma\gamma$. The $Z\gamma\gamma$ process has also been generated upon matching with an additional jet. The leading order (LO) cross-sections are obtained from MG5_aMC@NLO and the generation cuts for these background processes have been outlined in Appendix A.

We select events with exactly two b jets and two photons in the final state. The leading and the sub-leading (p_T ordered) b jets, b_1 and b_2 respectively, must carry $p_T > 30$ GeV and lie within a pseudorapidity range of $|\eta| < 4.0$. The two photons are also required to carry $p_T > 30$ GeV and must fall within a pseudorapidity coverage of $|\eta| < 4.0$. A veto is applied if any τ jets or isolated leptons (l , $l = e, \mu$) are present with $p_T > 20$ GeV and $|\eta| < 4.0$. This veto helps to reduce the $t\bar{t}h$ background where leptons can come from top decay. To offset the large $b\bar{b}\gamma\gamma^*$ background, we restrict the invariant mass of the photon pair ($m_{\gamma\gamma}$) to lie between 122 GeV and 128 GeV. We impose a lower cut on the ΔR ¹ between the photons and the b jets, $\Delta R_{b\gamma} > 0.2$, and require the invariant mass of the $b\bar{b}$ pair (m_{bb}) to be greater than 50 GeV to further tackle the QCD-QED $b\bar{b}\gamma\gamma^*$ background. The acceptance cuts have been summarized in Table 1. We would like to note that the generation level cuts have also been applied alongside the acceptance cuts.

The signal and background event samples, after being passed through the aforementioned cuts, are subjected to multivariate analysis using the BDTD algorithm, the XGBoost toolkit, and DNN, in order to discriminate between the background and signal samples and

¹The distance between two final state particles a and b in the $\eta - \phi$ plane is calculated as $\Delta R_{ab}^2 = \Delta\eta_{ab}^2 + \Delta\phi_{ab}^2$ where $\Delta\eta_{ab}$ and $\Delta\phi_{ab}$ are the differences in pseudorapidity and azimuthal angle of the particles a,b respectively.

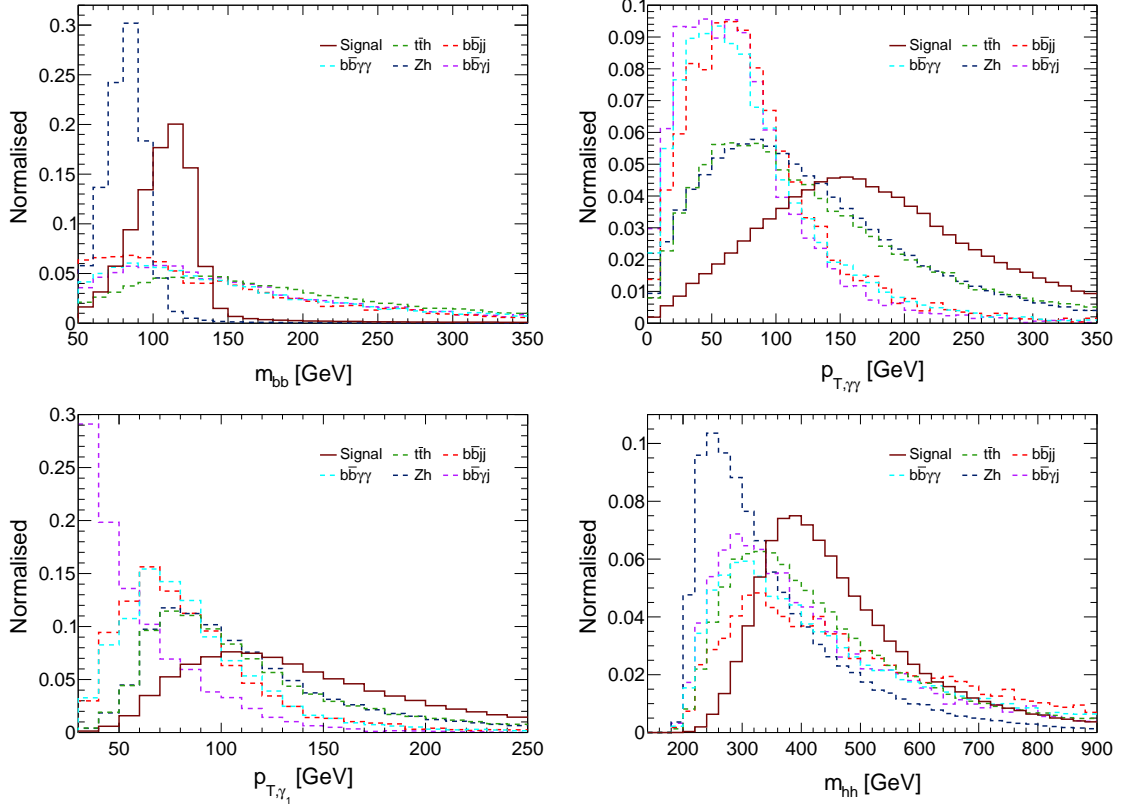


Figure 1: Normalized distributions of m_{bb} , $p_{T,\gamma\gamma}$, p_{T,γ_1} and m_{hh} for the $pp \rightarrow hh \rightarrow b\bar{b}\gamma\gamma$ signal and the dominant backgrounds after the acceptance cuts and the generation level cuts.

maximize the signal significance. The following 19 kinematic variables are used as inputs in the optimization procedure:

$$\begin{aligned}
 &m_{bb}, \Delta R_{\gamma\gamma}, \Delta R_{bb}, p_{T,bb}, p_{T,\gamma\gamma}, \Delta R_{bb\gamma\gamma}, p_{T,hh}, \Delta R_{b_i\gamma_i}, \\
 &m_{hh}, p_{T,b_{1,2}}, p_{T,\gamma_{1,2}}, \cancel{E}_T, \cos\theta^*, \cos\theta_{\gamma_1 h}
 \end{aligned} \tag{2.1}$$

Here, $p_{T,bb}$ and $p_{T,\gamma\gamma}$ represents the transverse momentum of the system of $b\bar{b}$ pair and the photon pair, respectively, while $\Delta R_{bb\gamma\gamma}$ represents the distance in the $\eta - \phi$ plane between the $b\bar{b}$ and $\gamma\gamma$ system. θ^* represents the angle between the outgoing photon and the Z -axis in the Collins-Soper (CS) frame [145, 146] and $\cos\theta^*$ is defined as:

$$\cos\theta^* = \frac{\text{Sinh}(\eta_{\gamma 1} - \eta_{\gamma 2})}{\sqrt{1 + (p_{T,\gamma\gamma}/m_{\gamma\gamma})^2}} \frac{2 p_{T,\gamma 1} p_{T,\gamma 2}}{m_{\gamma\gamma}^2} \tag{2.2}$$

The advantage of this variable is its less sensitivity to initial state radiations (ISR) in the CS frame. The final variable is $\cos\theta_{\gamma_1 h}$ where $\theta_{\gamma_1 h}$ represents the angle between the

direction of the leading p_T photon (γ_1) in the rest frame of the Higgs boson reconstructed from the diphoton system and the direction of the Higgs boson (reconstructed from the $\gamma\gamma$ system) in the lab frame. We must note that the numerical ordering of particles in our notation represents the p_T ordering with the subscript 1 assigned to the leading p_T object in its class.

	Process	Cross section order	Event yield after the analysis with		
			BDTD	XGBoost	DNN
Background	$t\bar{t}h$	NLO [147]	947	8×10^{-3}	7×10^{-3}
	$b\bar{b}\gamma\gamma^*$	LO	1328	266	1191
	<i>Fake</i> 1	LO	329	2.4	2.8
	<i>Fake</i> 2	LO	338	36	45
	Zh	NNLO (QCD) + NLO (EW) [147]	287	1149	615
	$b\bar{b}h$	LO	88	3×10^{-4}	0.21
	$Z\gamma\gamma$	LO	92	66	52
	hjj^*	LO	0.21	286	211
	Total		3410	1806	2117
Signal ($hh \rightarrow b\bar{b}\gamma\gamma$)		NNLO [148]	572	555	478
Significance (S/\sqrt{B})			9.8	13.1	10.4

Table 2: The signal and background yields at the HE-LHC along with the signal significance in the $b\bar{b}\gamma\gamma$ channel from the analysis using BDTD, XGBoost and DNN classifiers.

	Process	Event yield after the analysis with XGBoost with 95% probability cut
Background	$t\bar{t}h$	0.01
	$b\bar{b}\gamma\gamma^*$	2083
	<i>Fake</i> 1	4.6
	<i>Fake</i> 2	62
	Zh	1624
	$b\bar{b}h$	0.34
	$Z\gamma\gamma$	111
	hjj^*	419
	Total	4304
Signal ($hh \rightarrow b\bar{b}\gamma\gamma$)		636
Significance (S/\sqrt{B})		9.7

Table 3: The signal and background yields at the HE-LHC along with the signal significance for the $b\bar{b}\gamma\gamma$ channel upon applying the probability cut on the XGBoost output at 95%.

The kinematic variables which exhibited the maximal capability in discriminating the signal and background event samples during the BDTD optimization procedure are: m_{bb} , $p_{T,bb}$, p_{T,γ_1} and m_{hh} . The normalized distribution of these variables for the signal and

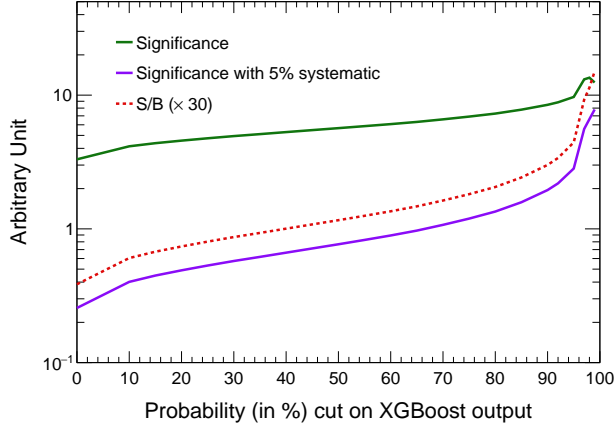


Figure 2: The variation of S/\sqrt{B} (with (5%) and without systematic uncertainty) and S/B is shown as a function of the probability cut on the XGBoost output for the $b\bar{b}\gamma\gamma$ channel.

the dominant background processes, after passing through the acceptance cuts and the generation cuts, are illustrated in Fig. 1. In Table 2, we show the signal and background yields together with the signal significance obtained from the multivariate BDTD analysis. The signal significance is calculated as S/\sqrt{B} , where, S is the signal yield and B is the total background yield. As shown in Table 2, the BDTD optimization yields a signal significance of 9.8 in the absence of any systematic uncertainty ($\sigma_{sys.un}$), exhibiting a roughly ~ 6 times improvement over its HL-LHC counterpart [101]. Upon assuming $\sigma_{sys.un} = 5\%$ ², the signal significance reduces to $S/\sqrt{B} \sim 4.0$, still within the projected exclusion reach ($> 2\sigma$) at the HE-LHC. We also show the signal and background yields, and the signal significance, obtained from the XGBoost optimization, in Table 2. The kinematic variables listed in Eqn. 2.1 have also been used in the multivariate analysis performed using the XGBoost toolkit. Here, we have applied the probability cut on the XGBoost output at 97% and we obtain a signal significance of 13.1. The signal and background yields from the DNN analysis are also listed in Table 2. The DNN training and optimization results in a signal significance of 10.39 which is slightly lower than the XGBoost estimation but larger than the BDTD output. We also list the signal and background yields, and the associated signal significance, obtained from the XGBoost analysis upon imposing the probability cut at 95% in Table 3. Reducing the probability cut from 97% to 95% reduces the signal significance to 9.7. It must also be noted that the yield of the dominant QCD-QED $b\bar{b}\gamma\gamma$ background increases from $\lesssim 1$ to 1633 when the probability cut on the XGBoost output is reduced from 97% to 95%. We would like to acknowledge that the choice of the probability cut is subjective and the results would differ with a different choice of the probability cut.

²With $N\%$ systematic uncertainty, the significance formula takes the form: $S/\sqrt{B + (0.01 * N * B)^2}$

Therefore, for the sake of completeness, we also illustrate the signal significance and the S/B value as a function of probability cut (in %) on the XGBoost output in Fig. 2. The solid green and purple lines in Fig. 2 represent the signal significance obtained by assuming zero and 5% systematic uncertainty, respectively. The dashed red line represents the ratio of signal over background, scaled by a factor of 30^3 .

2.2 The $b\bar{b}\tau\tau$ channel

Compared to the $b\bar{b}\gamma\gamma$ search channel, the $b\bar{b}\tau\tau$ final state suffers a drawback in terms of signal clarity, however, it gains a favorable stance on account of its considerably large production rate. An added advantage is the possibility to obtain three different final states depending on the decay modes of the τ leptons: fully leptonic ($b\bar{b}ll + \cancel{E}_T$), semi-leptonic ($b\bar{b}l\tau_h + \cancel{E}_T$) and fully hadronic ($b\bar{b}\tau_h\tau_h$). In a previous analysis [101] where we had studied the future reach of all three decay modes of $b\bar{b}\tau\tau$ channel at the HL-LHC, the fully hadronic decay mode had exhibited the strongest sensitivity. Keeping this observation in mind, in the current subsection we exclusively focus on studying the potential reach of di-Higgs searches at the HE-LHC in the fully hadronic decay mode: $pp \rightarrow hh \rightarrow b\bar{b}\tau_h\tau_h$. In similarity with the previous subsection, we perform a detailed multivariate collider analysis with the BDTD algorithm, XGBoost and DNN.

The $t\bar{t}$ process is the leading contributor to the background. In order to generate sufficient statistics of all relevant $t\bar{t}$ decay modes, we generate the event samples for fully leptonic, semi-leptonic, and fully hadronic decay modes of $t\bar{t}$, separately. The QCD-QED $pp \rightarrow b\bar{b}Z^*/\gamma^* \rightarrow b\bar{b}\tau\tau$ and the fake $b\bar{b}jj$ (when *jets* fake as a τ_h) processes also provides a sizable contribution to the background. Sub-dominant contributors to the background are: Zh , $b\bar{b}h$, $t\bar{t}h$, $t\bar{t}W$ and $t\bar{t}Z$. In the case of Zh , contributions can arise from $(Z \rightarrow b\bar{b})(h \rightarrow \tau^+\tau^-)$ as well as from $(Z \rightarrow \tau^+\tau^-)(h \rightarrow b\bar{b})$. The large cross-section of the background processes also demands a large event statistics. To efficiently achieve larger statistics, we impose hard cuts at the generation level which have been listed in Appendix A.

The substantial difference in the production cross-section of the signal and the dominant $t\bar{t}$ background necessitates the use of efficient kinematic variables to discriminate the two. The di-tau invariant mass ($m_{\tau\tau}$) is one such variable however the reconstruction of $m_{\tau\tau}$ at the LHC has always been wrapped with complications due to the accompanying \cancel{E}_T . A number of $\tau\tau$ reconstruction techniques have been studied and applied in previous analyses [149–151]. In the present work, we use the collinear mass approximation technique [151] to reconstruct $m_{\tau\tau}$. This technique assumes the following: the visible decay products and the neutrinos from a τ lepton are approximately collinear ($\theta_{vis} = \theta_\nu$, $\phi_{vis} = \phi_\nu$), and the neutrinos are the only source of \cancel{E}_T . Based on these assumptions, the x- and y-components of \cancel{E}_T can be defined as functions of the neutrino momenta, and individual contribution of

³The scaling has been done for illustrative reasons.

the neutrinos to the \cancel{E}_T can be ascertained upon solving these relations. We must note that this approximation technique is capable to reconstruct $m_{\tau\tau}$ correctly only under circumstances where the di-tau system is highly boosted and has recoiled against a hard object. This technique is applicable in the context of $pp \rightarrow hh \rightarrow b\bar{b}\tau\tau$ channel since the $h \rightarrow \tau\tau$ system is boosted against the $h \rightarrow b\bar{b}$ system. However, it is possible that this technique may overestimate the value of $m_{\tau\tau}$ when the \cancel{E}_T resolution is not accurate. Similar to our previous analysis [101], we consider modified lepton selection criteria following [152]. The total energy deposition of all the stable particles within $\Delta R_{\ell, \text{particle}} < 0.2$ of the electron or muon is required be at most 15 GeV. The tagging efficiency of a τ jet with $p_T > 20$ GeV and $|\eta| < 4.0$ is fixed at 55% and 50% [153] for one pronged and three pronged τ 's, respectively. Also, the rate of a light jet with $p_T > 20$ GeV and $|\eta| < 4.0$ getting mistagged as a τ tagged jet is assumed to be 0.35% [153].

We select events containing exactly two b -tagged *jets* and two τ -tagged *jets* in the final state. The b *jets* and the τ *jets* must carry $p_T > 30$ GeV and $p_T > 20$ GeV, respectively, and both must lie within a pseudorapidity range of $|\eta| < 4.0$. A veto is applied on events containing isolated leptons with $p_T > 20$ GeV and $|\eta| < 4.0$. Furthermore, the distance in the $\eta - \phi$ plane between the b *jets* (ΔR_{bb}), the τ *jets* ($\Delta R_{\tau_1\tau_2}$) and in between all possible pairs of b and τ *jets* ($\Delta R_{b_i\tau_j}$ ($i, j = 1, 2$)) is required to be greater than 0.2. Here, the superscripts 1 and 2 represents the p_T ordered leading and sub-leading objects. Additionally, we also impose the generation level cuts, *viz.* a lower limit on the invariant mass of the b *jets*, $m_{bb} > 50$ GeV and the invariant mass of the visible decay products of the τ 's, $m_{\tau\tau}^{\text{vis.}} > 50$ GeV.

The selected signal and background events are subjected to multivariate analysis with the following input kinematic variables:

$$p_{T,bb}, \Delta R_{bb}, m_{bb}, p_{T,\tau_h\tau_h}, \Delta R_{\tau_h\tau_h}, \Delta\phi_{\tau_{h1}\cancel{E}_T}, \Delta\phi_{\tau_{h2}\cancel{E}_T}, \\ m_{T,\tau_h\tau_h}, m_{\tau_h\tau_h}^{\text{col}}, m_{T2}, m_{\text{eff}}, \Delta R_{b_1\tau_{h1}}, p_{T,hh}^{\text{vis}}, m_{hh}^{\text{vis}}, \Delta R_{hh}^{\text{vis}}$$

where, $\Delta\phi_{\tau_{hi}\cancel{E}_T}$, $i = 1, 2$ is the difference between the azimuthal angle of the visible decay product of the τ and the \cancel{E}_T , $m_{T,\tau_h\tau_h}$ is the transverse mass of the τ pair and is defined by $m_{T,\tau_h\tau_h}^2 = (\sum_i E_{T,i})^2 - (\sum_i \vec{p}_{T,i})^2$ where i runs over the visible decay products of the τ and the \cancel{E}_T , m_{T2} is the stransverse mass [149, 150] and m_{eff} is the scalar sum of transverse momentum of all the visible decay products and \cancel{E}_T . The m_{T2} variable characterizes the topology of the fully leptonic $t\bar{t}$ background where the parent particles of the invisible neutrinos in the final state are of the same mass. In the case of fully leptonic $t\bar{t}$ background, it is bounded from above by the top quark mass, however, for the

	Process	Cross section order	Event yield after the analysis with		
			BDTD	XGBoost	DNN
Background	$t\bar{t}$ had	NNLO [154]	342	127	5.1
	$t\bar{t}$ semi-lep	NNLO [154]	29520	9037	11447
	$t\bar{t}$ lep	NNLO [154]	34914	5513	14701
	$b\bar{b}\tau\tau$	LO	26858	6055	1708
	$t\bar{t}h$	NLO [147]	3539	1180	1544
	$t\bar{t}Z$	NLO [155]	2217	443	652
	$t\bar{t}W$	LO	74	15	37
	$b\bar{b}h$	LO	18	9.8	4.7
	Zh	NNLO (QCD) + NLO (EW) [147]	1389	700	277
	$b\bar{b}jj$	LO	56388	18716	1315
Total			155260	41795	31690
Signal ($hh \rightarrow b\bar{b}\tau_h\tau_h$)			1088	981	760
Significance (S/\sqrt{B})			2.8	4.8	4.3

Table 4: The signal and background yields at the HE-LHC are shown along with the signal significance in the $b\bar{b}\tau^+\tau^-$ channel from the analysis using BDTD, XGBoost and DNN classifiers.

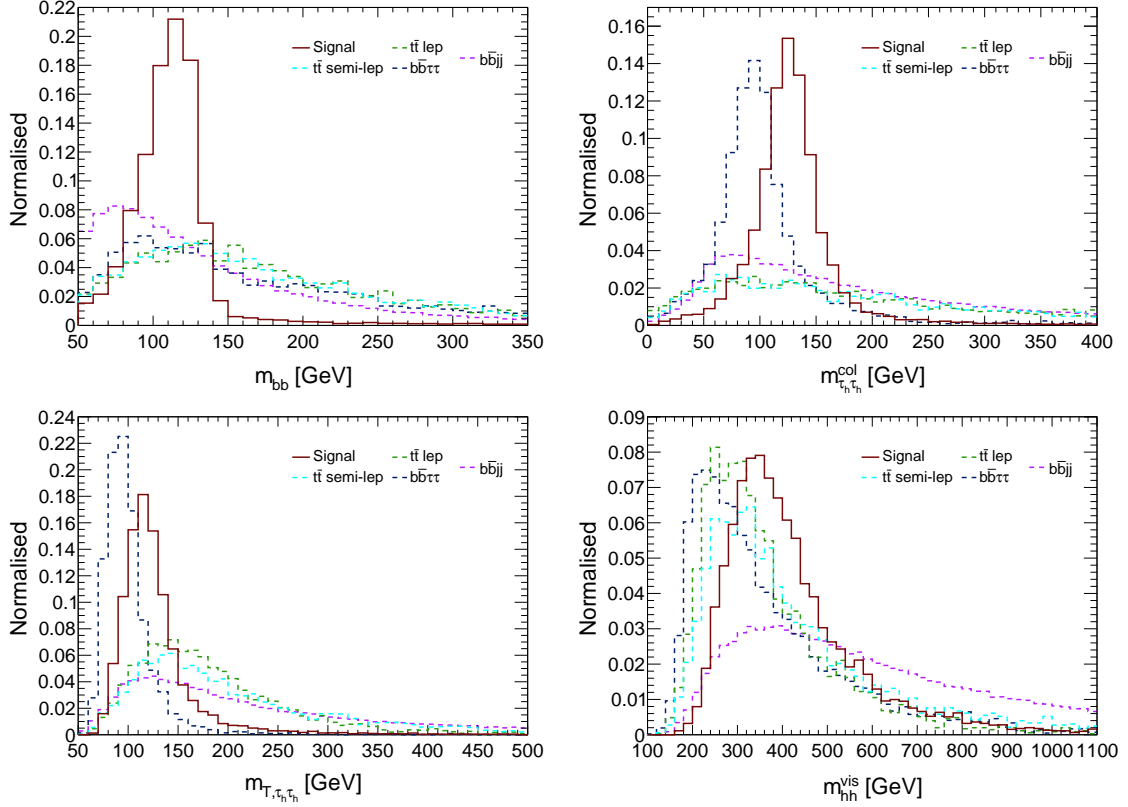


Figure 3: Normalized distributions of m_{bb} , $m_{\tau_h\tau_h}^{col}$, $m_{\tau_h\tau_h}$ and m_{hh}^{vis} for the $b\bar{b}\tau_h\tau_h$ signal and the dominant backgrounds after the acceptance cuts and the generation level cuts.

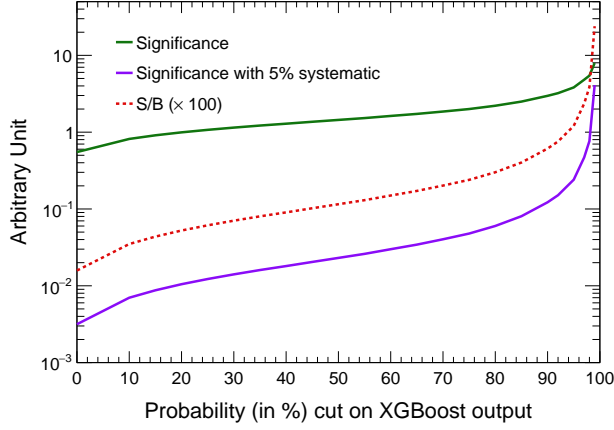


Figure 4: The variation of S/\sqrt{B} (with (5%) and without systematic uncertainty) and S/B is shown as a function of the probability cut on the XGBoost output for the $b\bar{b}\tau^+\tau^-$ channel.

$pp \rightarrow hh \rightarrow b\bar{b}\tau^+\tau^-$ signal, m_{T2} remains unbounded from above. In the construction of m_{T2} , the visible components are composed of two b jets and the two τ -tagged jets in the final state, while the invisible component is composed of the total \cancel{E}_T of the system. The other variables have their usual meaning. The kinematic variables which are most efficient in discriminating the signal and the backgrounds in the BDTD optimization are: m_{bb} , $m_{\tau_h\tau_h}^{col}$, $m_{T,\tau_h\tau_h}$ and m_{hh}^{vis} , and we illustrate their normalized distribution for the signal and the most dominant backgrounds in Fig. 3. The BDTD optimization results in a total background yield of 1.6×10^5 and a signal yield of 1088 leading to a signal significance of 2.8 assuming zero systematic uncertainty (see Table 4) and thus falls within the potential exclusion reach at the HE-LHC. We must however mention that S/B value of this channel is of the order of 10^{-2} and the signal significance drops considerably upon introducing systematic uncertainties.

The signal and background discrimination is also performed using XGBoost and DNN, and the respective signal and background yields are shown in Table 4. The signal and background yields for XGBoost are computed with a probability cut on the XGBoost output at 97%. The XGBoost signal yield is almost comparable to the signal yield from BDTD, however, the background yield is roughly $\sim 70\%$ less than its BDTD counterpart. Correspondingly, the signal significance improves to 4.8. In Fig. 4, we illustrate the variation of the signal significance obtained from the analysis using XGBoost, for 0% (solid green line) and 5% (solid purple line) systematic uncertainty, as a function of the probability cut on the XGBoost output. The red-dashed line represents the S/B value scaled with 10^2 . The analysis using DNN results in a signal significance of 4.27. Similar to our results in the $b\bar{b}\gamma\gamma$ channel (Sec. 2.1), we obtain the highest signal significance from XGBoost followed

by DNN and BDTD. However, we would like to mention that more efficient optimization of the DNN analysis may lead to improved signal-background discrimination leading to comparable results with XGBoost.

2.3 The $b\bar{b}WW^*$ channel

The $b\bar{b}WW^*$ channel manifests into three different final states: the fully leptonic $b\bar{b}l^+l^- + \cancel{E}_T$, the semi-leptonic $b\bar{b}l + jets + \cancel{E}_T$ and the fully hadronic $b\bar{b} + jets + \cancel{E}_T$. Among these three, the fully leptonic final state is relatively cleaner, has a smaller background, and therefore, is the focus of this study.

The leading and sub-leading contribution to the background comes from leptonically decaying $t\bar{t}$ and $llb\bar{b}$, respectively. Lesser contributions to the background arises from $t\bar{t}h$, $t\bar{t}Z$, $t\bar{t}W$ and tW . The tW process has been generated by merging with an additional *jet* and the W boson has been decayed leptonically. Furthermore, a hard cut of $m_{bb} \geq 50$ GeV is imposed at the generation level of $t\bar{t}$, $llb\bar{b}$ and tW processes. We have listed all such generation level cuts in Appendix A.

The event selection criteria requires the presence of exactly two b *jets* with $p_T > 30$ GeV and $|\eta| < 4.0$, and two oppositely charged isolated leptons with $p_T > 20$ GeV and $|\eta| < 4.0$. In addition, for the sake of consistency, the generation level hard cuts: $\Delta R_{b_i l_j} > 0.2$ ($i, j = 1, 2$) and $m_{bb} > 50$ GeV, imposed on $t\bar{t}$, $llb\bar{b}$ and tW , are applied on the signal and all the backgrounds at the selection level. The signal and the background samples thus obtained at the selection level are then passed through the BDTD algorithm. The following variables are considered to perform the multivariate analysis:

$$\begin{aligned} \log T, \log H, M_{T2}^{(b)}, M_{T2}^{(\ell)}, \sqrt{\hat{s}_{min}^{(\ell\ell)}}, \sqrt{\hat{s}_{min}^{(bb\ell\ell)}}, p_{T,\ell_{1/2}}, \cancel{E}_T, m_{\ell\ell}, m_{bb}, \\ \Delta R_{\ell\ell}, \Delta R_{bb}, p_{T,bb}, p_{T,\ell\ell}, \Delta\phi_{bb\ell\ell}. \end{aligned} \quad (2.3)$$

Here, T and H refers to Topness and Higgsness [94, 156], respectively. The Topness variable is designed to characterize the fully-leptonic $t\bar{t}$ topology. The leptonic $t\bar{t}$ final state has two neutrinos whose three momenta are undetermined resulting in 6 unknowns. Four on-shell mass conditions are provided by m_t , $m_{\bar{t}}$, m_{W^+} and m_{W^-} . The three-momenta of the neutrino is fixed by minimizing χ_{ij}^2 which is defined as [94]:

$$\chi_{ij}^2 \equiv \min_{\vec{p}_T = \vec{p}_{\nu T} + \vec{p}_{\bar{\nu} T}} \left[\frac{(m_{b_i \ell^+ \nu}^2 - m_t^2)^2}{\sigma_t^4} + \frac{(m_{\ell^+ \nu}^2 - m_W^2)^2}{\sigma_W^4} + \frac{(m_{b_j \ell^- \bar{\nu}}^2 - m_t^2)^2}{\sigma_t^4} + \frac{(m_{\ell^- \bar{\nu}}^2 - m_W^2)^2}{\sigma_W^4} \right]. \quad (2.4)$$

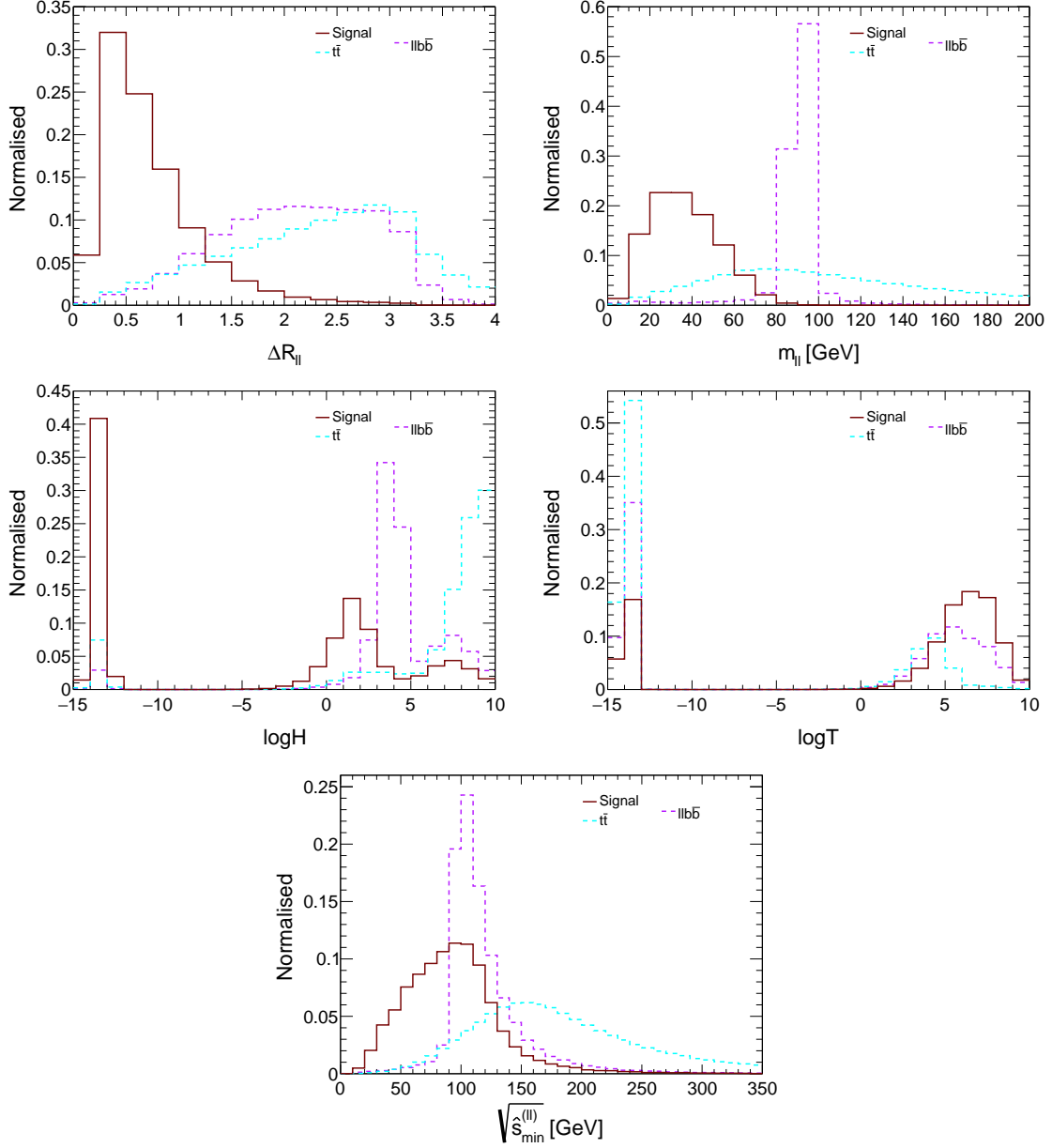


Figure 5: Normalized distributions of $\Delta R_{\ell\ell}$, $m_{\ell\ell}$, $\log H$, $\log T$ and $\sqrt{\hat{s}_{\min}^{(\ell\ell)}}$ for the $b\bar{b}WW^* \rightarrow 2b2\ell + \cancel{E}_T$ signal and dominant backgrounds after the acceptance cuts and the generation level cuts.

Here, i, j can take values of 1 or 2, corresponding to the leading (b_1) or sub-leading (b_2) p_T ordered b jet, respectively. Following Ref. [94], we take $\sigma_t = \sigma_W = 5$ GeV. The minimization of χ_{ij}^2 is performed under the condition that the total missing transverse momentum of the system is the sum of the transverse momentum of the two neutrinos, $\vec{p}_T = \vec{p}_{\nu T} + \vec{p}_{\bar{\nu} T}$. There can be two different combinations of the b jet, lepton and the neutrino: $b_1 l^+ \nu$ and $b_2 l^- \bar{\nu}$, or $b_2 l^+ \nu$ and $b_1 l^- \bar{\nu}$. The Topness is eventually defined by considering

the minimum of the two χ_{ij}^2 values, $T = \min(\chi_{12}^2, \chi_{21}^2)$. Similarly, the Higgsness variable targets the $h \rightarrow WW^*$ topology in the signal and is defined as [94]:

$$H \equiv \min \left[\frac{(m_{\ell^+\ell^-\nu\bar{\nu}}^2 - m_h^2)^2}{\sigma_{h\ell}^4} + \frac{(m_{\nu\bar{\nu}}^2 - m_{\nu\bar{\nu},peak}^2)^2}{\sigma_\nu^4} + \right. \\ \left. \min \left(\frac{(m_{\ell^+\nu}^2 - m_W^2)^2}{\sigma_W^4} + \frac{(m_{\ell^-\bar{\nu}}^2 - m_{W^*,peak}^2)^2}{\sigma_{W^*}^4}, \frac{(m_{\ell^-\bar{\nu}}^2 - m_W^2)^2}{\sigma_W^4} + \frac{(m_{\ell^+\nu}^2 - m_{W^*,peak}^2)^2}{\sigma_{W^*}^4} \right) \right]. \quad (2.5)$$

Here, $m_{W^*,peak}$ is the invariant mass of the off-shell W boson produced from the decay of the Higgs boson. $m_{W^*,peak}$ is defined as:

$$\frac{1}{\sqrt{3}} \sqrt{2(m_h^2 + m_W^2) - \sqrt{m_h^4 + 14m_h^2 m_W^2 + m_W^4}} \quad (2.6)$$

$m_{\nu\bar{\nu},peak}$ in Eqn. 2.5 corresponds to the location of the peak of the $\nu\bar{\nu}$ invariant mass distribution, and is allocated a value of 30 GeV following Ref. [94]. We also fix σ_{W^*} , $\sigma_{h\ell}$ and σ_ν at 5 GeV, 2 GeV and 10 GeV, respectively, following Ref. [94]. A combination of these two variables is found to be effective in discriminating the large $t\bar{t}$ background from the signal. The b jets and the decay products of the W boson correspond to the visible and invisible components, respectively, of the $m_{T2}^{(b)}$ variable, while $m_{T2}^{(\ell)}$ is computed by considering the two isolated final state leptons to form the visible component and the neutrinos to form the invisible component. These two variables have been taken from [157]. We also consider the minimum of the Mandelstam invariant mass variable: $\sqrt{\hat{s}_{min}}$ [157], where $\sqrt{\hat{s}_{min}^{(ab)}}$ represents the minimum value of the centre of mass (c.o.m) energy required to produce the parton level parent particles of the final state particles a and b . It is defined as:

$$\hat{s}_{min}^{(ab)} = m_{ab}^2 + 2(\sqrt{|p_T^{ab}|^2 + m_{ab}^2} p_T - \vec{p}_T^{ab} \cdot \vec{p}_T)$$

where m_{ab} and p_T^{ab} are the invariant mass and transverse momentum, respectively, of the visible system ab . In the present scenario, we consider two such variables: $\sqrt{\hat{s}_{min}^{(\ell\ell)}}$ and $\sqrt{\hat{s}_{min}^{(bb\ell\ell)}}$, where the former and the latter variables represent the minimum c.o.m. energy scale of the parton level WW^* pair and the Higgs pair, respectively. Furthermore, in Eqn. 2.3, $p_{T,\ell_{1/2}}$ represents the p_T of the leading and sub-leading isolated leptons (represented as l_1 and l_2 , respectively), $m_{\ell\ell}$ represents the invariant mass of the $l_1 l_2$ pair, $\Delta R_{\ell\ell}$ corresponds to the distance between l_1 and l_2 in the $\eta - \phi$ plane, $p_{T,\ell\ell}$ measures the p_T of the di-lepton system and $\Delta\phi_{bb\ell\ell}$ computes the difference of azimuthal angles between the $b\bar{b}$ system and the di-lepton system.

The variables which are found to be most efficient in discriminating the signal and the background in the BDTD analysis are: $\Delta R_{\ell\ell}$, $m_{\ell\ell}$, $\log H$ and $\log T$. We illustrate the

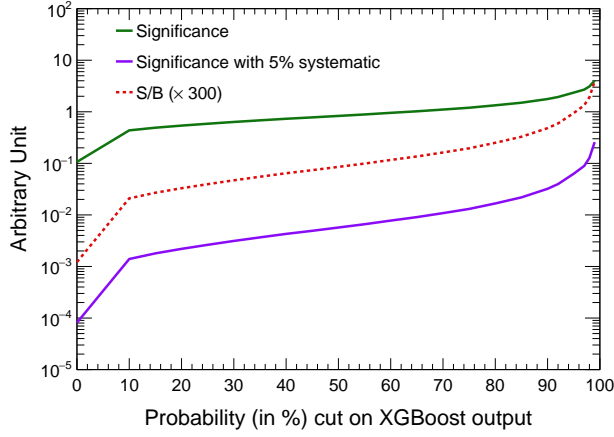


Figure 6: The variation of S/\sqrt{B} (with (5%) and without systematic uncertainty) and S/B is shown as a function of the probability cut on the XGBoost output for the $b\bar{b}WW^*$ final state.

normalized distributions of these four variables and $\sqrt{\hat{s}_{min}^{(\ell\ell)}}$, for the signal and the dominant backgrounds: $t\bar{t}$ and $\ell\ell b\bar{b}$, in Fig. 5. The signal and background yields obtained from the BDTD analysis have been listed in Table 5. We obtain a signal significance of 1.5 without assuming any systematic uncertainties. We must note that the signal significance value undergoes a significant reduction upon the introduction of systematic uncertainty due to the small S/B .

	Process	Cross section order	Event yield after the analysis with		
			BDTD	XGBoost	DNN
Background	$t\bar{t}$ lep	NNLO [154]	374866	305038	242560
	$\ell\ell b\bar{b}$	LO	142386	48365	22441
	$t\bar{t}Z$	NLO [155]	8084	3364	1930
	$t\bar{t}h$	NLO [147]	5598	7636	2960
	$t\bar{t}W$	LO	661	775	280
	tW	LO	4.3	6.5	3.7
	Total		531600	365185	270175
Signal ($hh \rightarrow b\bar{b}WW^* \rightarrow b\bar{b}\ell\ell + \cancel{E}_T$)		NNLO [148]	1107	1661	746
Significance (S/\sqrt{B})			1.5	2.7	1.4

Table 5: The signal and background yields at the HE-LHC along with the signal significance for the $b\bar{b}WW^*$ channel from the analysis using BDTD, XGBoost and DNN classifiers.

Here again, we also use the XGBoost and DNN classifier to perform a detailed collider analysis. We obtain a signal yield of 1661 (746) and a total background yield of 3.6×10^5 (2.7×10^5) resulting in a signal significance of 2.7 (1.4) which is ~ 1.8 (~ 0.95) times

higher (smaller) than the corresponding value from the BDTD optimization (see Table. 5). We would like to mention that signal yields from the BDTD optimization and the XGBoost toolkit are roughly within 5% of each other, however, the XGBoost classifier performs background rejection more efficiently. The XGBoost background yield is approximately 30% smaller than its BDTD counterpart. The XGBoost signal significance, computed assuming zero and 5% systematic uncertainty, are also illustrated in Fig. 6 as a function of the probability cut applied on the XGBoost output, in solid green and solid purple lines, respectively. The red dashed line in Fig. 6 represents the respective variation in the value of S/B (scaled with 300).

2.4 The $WW^*\gamma\gamma$ channel

The production rate of $pp \rightarrow hh \rightarrow WW^*\gamma\gamma$ is smaller than the di-Higgs final states considered until now. However, the $WW^*\gamma\gamma$ channel draws an advantage from its relatively smaller backgrounds. In the present subsection, we focus only on the pure leptonic decay mode of $WW^*\gamma\gamma$ and defer the treatment of the semi-leptonic and hadronic decay modes to a future study. The pure leptonic decay mode results in the $WW^*\gamma\gamma \rightarrow l^+l^-\gamma\gamma + \cancel{E}_T$ final state. In the analysis channels studied until now, we had performed the signal-background discrimination through the BDTD optimization, the XGBoost toolkit as well as the DNN framework. In all the previous channels, namely $b\bar{b}\gamma\gamma$, $b\bar{b}\tau^+\tau^-$ and $b\bar{b}WW^*$, we observed that the DNN analysis resulted in a slight weaker signal significance than the XGBoost classifier. Therefore, present subsection onwards, we perform the collider analysis only through the BDTD algorithm and the XGBoost toolkit.

The dominant source of background is the $t\bar{t}h$ process. Sub-dominant contributions arise from Zh and $ll\gamma\gamma$ processes. The later two backgrounds have been generated upon merging with two additional *jets* and one additional *jet*, respectively. At the generation level, we impose a lower limit on the invariant mass of the di-lepton pair, $m_{ll} > 20$ GeV, and a lower limit on the distance between the two final state leptons and the photons in the $\eta - \phi$ plane, $\Delta R_{ll/\gamma\gamma} > 2.0$. Additionally, the invariant mass of the photon pair, $m_{\gamma\gamma}$, is also restricted between $120 \text{ GeV} < m_{\gamma\gamma} < 130 \text{ GeV}$ at the generation level. The generation level cuts have been listed in Appendix A.

An event is required to have two isolated opposite sign leptons (electrons or muons) with $p_T \geq 30$ GeV and two photons with $p_T \geq 20$ GeV. The leptons and photons must lie within $|\eta| \leq 4.0$. To tackle the $t\bar{t}h$ background, a b *jet* veto is applied. In addition to these acceptance cuts, the generation level cuts are also imposed. We also veto events containing τ *jets* and demand $m_{\gamma\gamma}$ to lie within $[122 : 128] \text{ GeV}$. We perform a multivariate analysis with the BDTD algorithm and the XGBoost toolkit using the following kinematic variables:

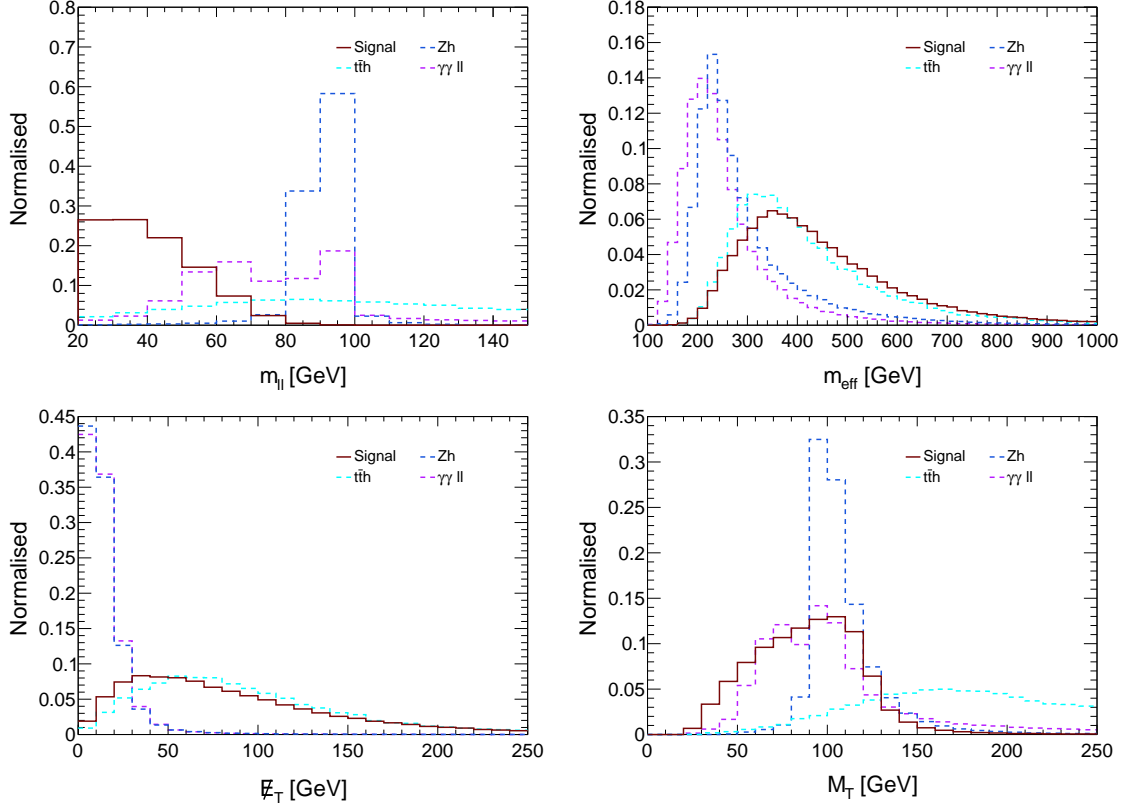


Figure 7: Normalized distributions of $m_{\ell\ell}$, m_{eff} , E_T and M_T for the $WW^*\gamma\gamma \rightarrow 2\ell 2\gamma + E_T$ signal and the dominant backgrounds after the application of acceptance cuts and generation level cuts.

$$p_{T,\gamma\gamma}, \Delta R_{\gamma\gamma}, m_{\ell\ell}, p_{T,\ell\ell}, \Delta R_{\ell\ell}, \Delta R_{\ell\ell\gamma\gamma}, M_T, p_{T,hh}, m_{\text{eff}}, \Delta R_{\gamma_1\ell_1}, \cos\theta^*, \cos\theta_{\gamma_1h}, E_T \quad (2.7)$$

Here, M_T refers to the transverse mass of the $h \rightarrow WW^* \rightarrow l^+l^- + E_T$ system while m_{eff} represents the sum of the visible transverse momentum (H_T) and E_T in the event. The variables which are most efficient in discriminating the signal and background events in the BDTD analysis are: $m_{\ell\ell}$, m_{eff} , E_T and M_T , and we illustrate their normalized distributions in Fig. 7.

The signal and background yields obtained from the BDTD and the XGBoost optimization (with probability cut at 97%) are listed in Table 6 along with the respective signal significance values (assuming zero systematic uncertainty). The S/B value for this channel is ~ 0.2 (from BDTD) and ~ 0.3 (from XGBoost), and are only behind the S/B values from $b\bar{b}\gamma\gamma$ search channel. The signal yields from both the optimizations are roughly similar however the background yield from XGBoost is $\sim 30\%$ smaller. We obtain a signal

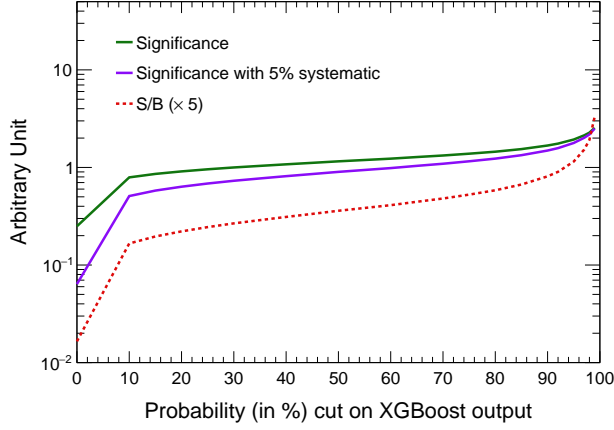


Figure 8: The variation of S/\sqrt{B} (with (5%) and without systematic uncertainty) and S/B is shown as a function of the probability cut on the XGBoost output for the $WW^*\gamma\gamma$ channel.

significance of 1.7 through BDTD analysis while the XGBoost framework leads to a signal significance of 2.1. We follow the color code of Fig. 2 and illustrate the signal significances computed at zero and 5% systematic uncertainty as a function of the probability cut on the XGBoost output in Fig. 8. The relatively large S/B value in the present channel is reflected by the red dashed line in Fig. 8.

	Process	Cross section order	Event yield after the analysis with	
			BDTD	XGBoost
Background	$t\bar{t}h$	NLO (QCD + EW) [147]	46	33
	Zh + jets	NNLO (QCD) + NLO (EW) [147]	6.9	5.2
	$\ell\ell\gamma\gamma$ + jet	LO	18	11
	Total		71	49
Signal ($hh \rightarrow \gamma\gamma WW^* \rightarrow \gamma\gamma\ell\ell + \cancel{E}_T$)		NNLO [148]	14	15
Significance (S/\sqrt{B})			1.7	2.1

Table 6: The signal and background yields at the HE-LHC along with the signal significance for the $WW^*\gamma\gamma$ channel from the analysis using BDTD and XGBoost classifiers.

2.5 The $b\bar{b}ZZ^*$ channel

In this subsection, we study the potential reach of the largely unexplored $b\bar{b}ZZ^*$ channel. We study two different final states emerging from the leptonic decay of the Z/Z^* bosons. In the first category, we consider the scenario where both the Z bosons decay into electrons or muons (collectively represented as l') resulting in $2b4l'$ final state while in the second

category we consider the scenario where one of the Z bosons decay into a pair of electrons while the other decays into muons leading to $2b2e2\mu$ final state, *viz.*

$$pp \rightarrow hh \rightarrow b\bar{b}ZZ^* \rightarrow b\bar{b} 4l', \quad l' = e^\pm \text{ or } \mu^\pm$$

$$pp \rightarrow hh \rightarrow b\bar{b}ZZ^* \rightarrow b\bar{b} e^+e^-\mu^+\mu^-$$

The most dominant contribution to the background comes from $t\bar{t}h$. We must note that the inclusive production of $t\bar{t}h$ predominantly populates the hadronic final states over the leptonic states due to larger branching rates. Therefore, in order to generate a sufficiently large statistics of the specific final states emerging from $t\bar{t}h$ which are more relevant background sources to the $2b4l'$ and $2b2e2\mu$ signal channels, the background generation is divided into six different categories. In the first three categories, the h undergoes decay via $h \rightarrow ZZ^* \rightarrow 4l (l = e, \mu, \tau)$ while the top pairs are decayed leptonically, semi-leptonically and hadronically, respectively. In the fourth category, the $t\bar{t}$ pair is leptonically decayed while the h undergoes decay via $h \rightarrow ZZ^* \rightarrow (Z/Z^* \rightarrow 2l)(Z^*/Z \rightarrow b\bar{b}/jj/\nu\bar{\nu})$. In the last two categories, h undergoes decay into WW^* and $\tau^+\tau^-$, respectively, while the top pair undergoes leptonic decay. In order to compute the overall background contribution from $t\bar{t}h$, the weighted sum of the six categories is considered. Sub-leading contribution to the background arises from Zh , $t\bar{t}Z$ and Higgs production in association with $b\bar{b}$ through gluon fusion ($ggF - b\bar{b}h$). Numerous fake backgrounds also contribute, *viz.* $ggF - c\bar{c}h$, Wh , Whc and higgs production through vector boson fusion ($VBF - hjj$). These processes contribute to the overall background yield when the c jets or the light jets get faked as b jets. Hard cuts have been applied at the generation level of these backgrounds and those have been listed in Appendix A.

Before presenting the results from our collider analysis in the $2b4l'$ and $2b2e2\mu$ channels, we briefly discuss the parton level kinematics of the final state leptons at $\sqrt{s} = 27$ TeV. We illustrate the normalized distribution of the transverse momenta of the four leptons, $l_{1,2,3,4}$, with l_1 being the highest and l_4 being the lowest p_T lepton. We would like to emphasize that the transverse momentum carried by the final state leptons is relatively small even at a $\sqrt{s} = 27$ TeV proton-proton collider. The p_{T,l_1} distribution for the signal peaks at a slightly larger value (~ 65 GeV) compared to the backgrounds, all of which peak roughly below 50 GeV. The peak of the p_{T,l_2} and p_{T,l_3} distributions for the signal and the backgrounds fall roughly within a similar range, while the peak of p_{T,l_4} for the signal and the backgrounds is located below ~ 5 GeV. These observations are important while choosing the trigger cuts at the event selection level.

In the following subsections, we study the projected potential of observing the non-resonant di-Higgs signal in the $2b4l'$ and $2b2e2\mu$ channel at the HE-LHC, and detail the results from the BDTD optimization and the analysis using XGBoost toolkit.

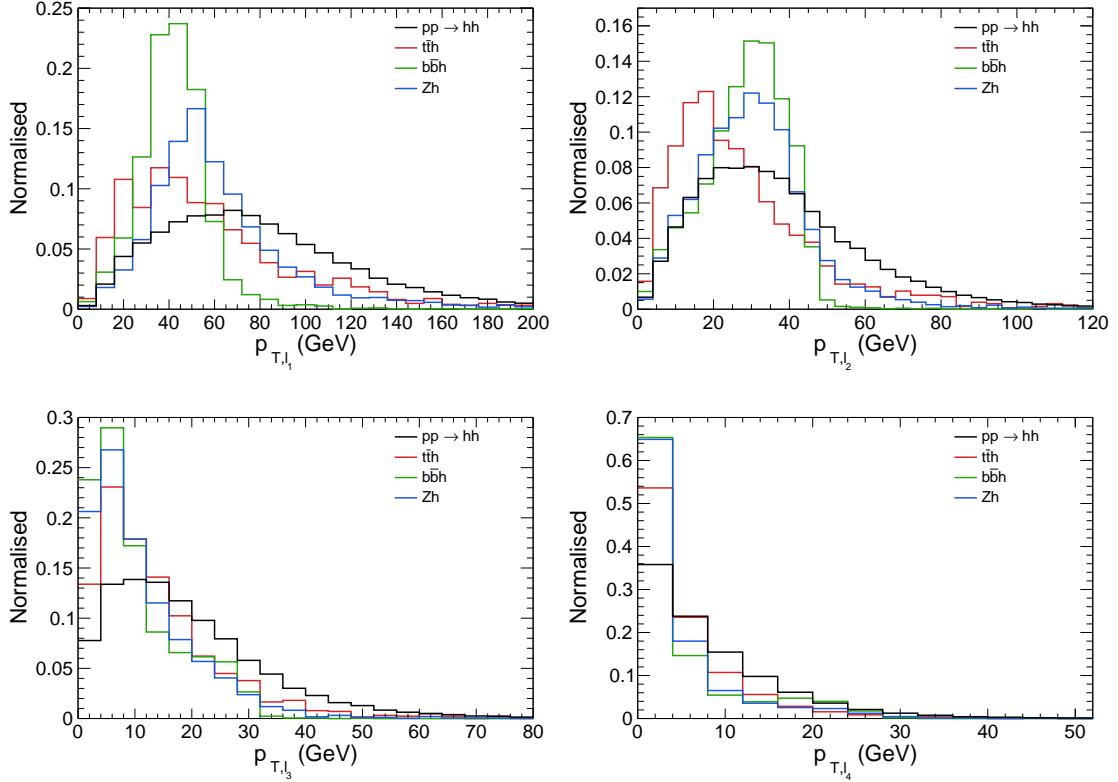


Figure 9: Normalized distribution of the transverse momentum, p_T , of the four leptons produced via: $pp \rightarrow hh \rightarrow b\bar{b}ZZ^* \rightarrow b\bar{b}(ZZ^* \rightarrow 4l)$, at the parton level.

2.5.1 The $2b4l'$ channel

The selected events are required to have exactly two b tagged *jets* with $p_T > 20$ GeV and $|\eta| < 4.0$, and four isolated l' 's carrying $p_T > 5$ GeV within $|\eta| < 4.0$. The invariant mass of the four leptons is also restricted between 120 GeV and 130 GeV. In addition, ΔR_{bb} is required to be greater than 0.2 and m_{bb} must be > 50 GeV. We must note that it is possible to construct four different combinations of same flavor opposite sign (SFOS) l' pairs. Thus, the Z and Z^* can be reconstructed in two different ways. We represent these two possibilities with superscript 1 and 2. If we represent the two Z bosons as Z_1 and Z_2 , then the two different SFOS pairs would result in either (Z_1^1, Z_2^1) or (Z_1^2, Z_2^2) . We utilize kinematic variables constructed from both, Z^1 and Z^2 , in performing the collider analysis. First, we perform a multivariate analysis with BDTD algorithm and subsequently, we also perform signal optimization with XGBoost with the aim to maximize the signal significance. The following kinematic variables are used as inputs to the analysis techniques:

$$p_{T,bb}, \Delta R_{bb}, m_{bb}, p_{T,4\ell}, m_{Z_i}^{1,2}, \Delta R_{ZZ}^{1,2}, m_{T2}, m_{\text{eff}}, \Delta R_{b_1\ell_1}, m_{hh}, \Delta R_{hh}, \cancel{E}_T$$

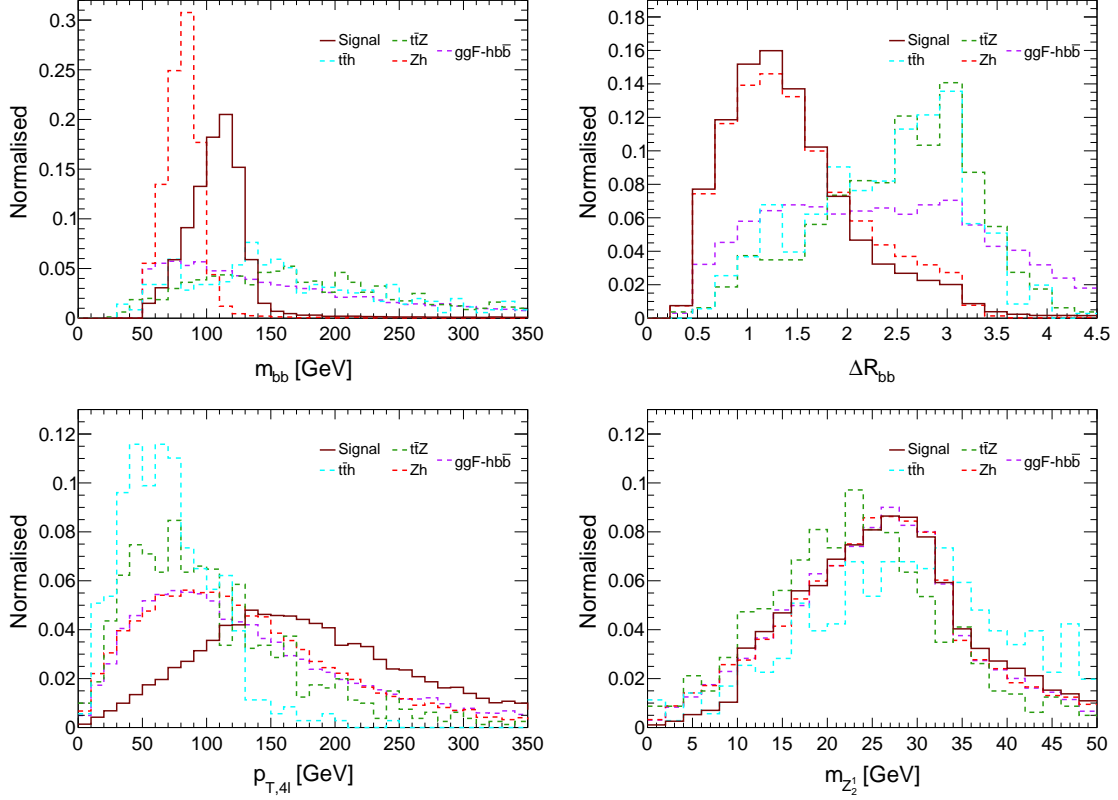


Figure 10: Normalized distributions of m_{bb} , ΔR_{bb} , $p_{T,4l}$ and $m_{Z_2^1}$ for the $2b4l'$ signal and the dominant backgrounds after the acceptance cuts and the generation level cuts.

Here, $m_{Z_i^1}$ and $m_{Z_i^2}$, with $i = 1, 2$, corresponds to the invariant mass of the four reconstructed Z bosons as discussed previously, ΔR_{ZZ}^1 represents the ΔR value between Z_1^1 and Z_2^1 , and ΔR_{ZZ}^2 represents the ΔR value between Z_1^2 and Z_2^2 . The other variables have their usual meanings. m_{bb} , ΔR_{bb} , $p_{T,4l'}$ and $m_{Z_2^1}$ are found to be the variables which are most efficient in discriminating the signal and the background through BDTD optimization. We illustrate their normalized distribution in Fig. 10.

The signal and background yields obtained from the BDTD analysis and the XGBoost analysis are presented in Table 7. The corresponding signal significance is also listed. We observe a background yield of 18.4 and a signal yield of 4.03 from the BDTD analysis resulting in a signal significance of 0.94. We must also note that this channel registers an impressive S/B value of 0.22. The analysis using XGBoost gives a background yield of 49.4 and a signal yield of 6.7 leading to a signal significance of 0.96. Here, we have imposed the probability cut on the XGBoost output at 95%. Imposing the probability cut at 97% leads to an improved signal significance of 1.9. We show the variation of S/\sqrt{B} and S/B

	Process	Cross section order	Event yield after the analysis with	
			BDTD	XGBoost (probability cut > 95%)
Background	$t\bar{t}h$	NLO [147]	9.9	32
	$t\bar{t}Z$	NLO [155]	1.1	4.9
	Zh	NNLO (QCD) + NLO (EW) [147]	5.6	8.5
	Wh	NNLO (QCD) + NLO (EW) [147]	2×10^{-3}	3×10^{-3}
	Whc	LO	4×10^{-4}	9×10^{-4}
	$ggF\text{-}h\bar{b}b$	LO	1.8	3.5
	$ggF\text{-}hc\bar{c}$	LO	4×10^{-3}	8×10^{-3}
	$VBF\text{-}hjj$	NNLO (QCD) + NLO (EW) [147]	1×10^{-4}	4×10^{-4}
Total			18	49
Signal ($hh \rightarrow b\bar{b}ZZ^* \rightarrow 2b4lep$)		NNLO [148]	4.0	6.7
Significance (S/\sqrt{B})			0.94	0.96

Table 7: The signal and background yields at the HE-LHC along with the signal significance for the $b\bar{b}ZZ^* \rightarrow 2b4l'$ channel from the analysis using the BDTD and the XGBoost classifiers.

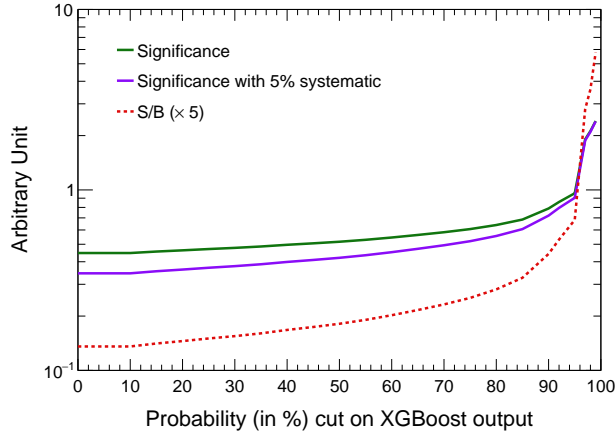


Figure 11: The variation of S/\sqrt{B} (with (5%) and without systematic uncertainty) and S/B is shown as a function of the probability cut on the XGBoost output for the $b\bar{b}ZZ^* \rightarrow b\bar{b} 4l'$ channel.

as a function of the probability cut on the XGBoost output in Fig. 11 following the color code of Fig. 2.

2.5.2 The $2b2e2\mu$ channel

The event selection criteria requires the presence of exactly two b jets with $p_T > 20$ GeV and $|\eta| < 4.0$, two isolated electrons and two isolated muons with $p > 5$ GeV and $|\eta| < 4.0$. Similar to the selection cuts prescribed in Sec. 2.5.1, we apply $\Delta R_{bb} > 0.2$ and $m_{bb} > 50$ GeV. Furthermore, we also demand that the invariant mass of the $2e2\mu$ system ($m_{2e2\mu}$) must lie within 120 GeV and 130 GeV. In the present scenario, the two electrons and the muons are combined, respectively, to reconstruct the Z bosons. Among the two Z

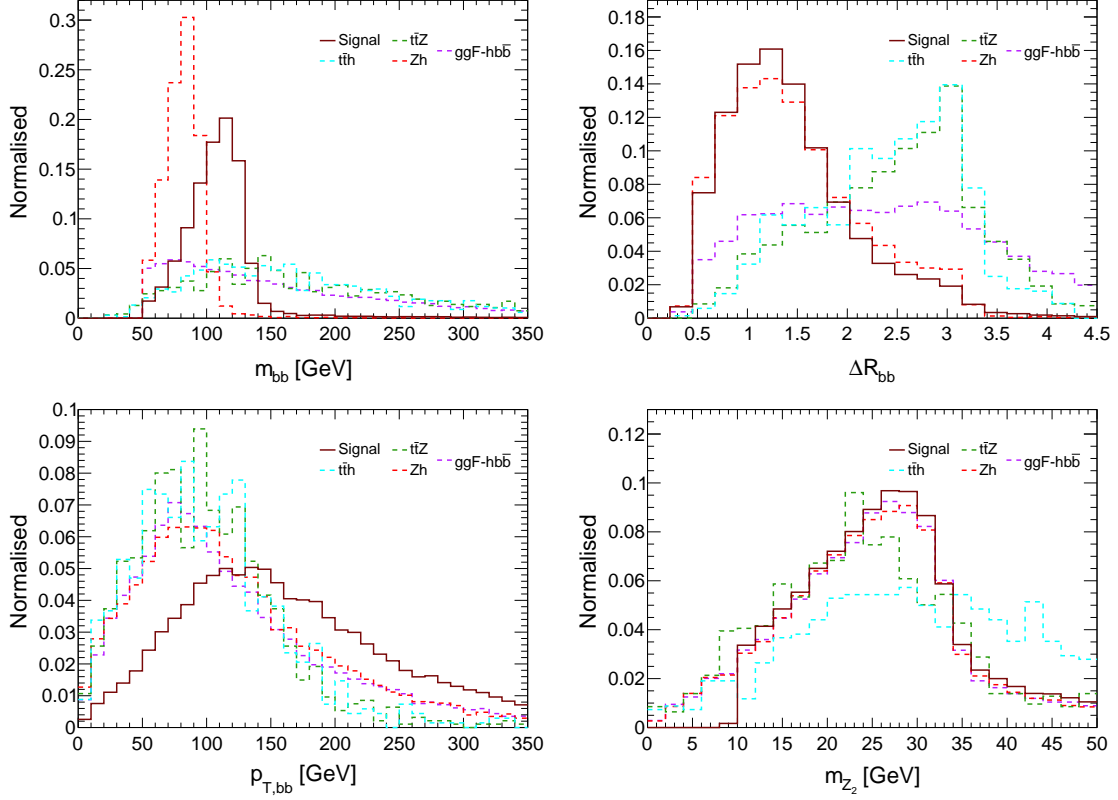


Figure 12: Normalized distributions of m_{bb} , ΔR_{bb} , $p_{T,bb}$ and m_{Z_2} for the $2b2e2\mu$ signal and the dominant backgrounds after the acceptance cuts and the generation level cuts.

bosons, the one with invariant mass closest to m_Z will be referred to as Z_1 while the other Z boson will be referred as Z_2 .

The signal and background events which pass the selection cuts are subjected to multivariate analysis using the BDTD algorithm and the XGBoost package. In this regard, we consider the following 13 kinematic variables:

$$p_{T,bb}, \Delta R_{bb}, m_{bb}, p_{T,2e2\mu}, m_{Z_i}, \Delta R_{ZZ}, m_{T2}, m_{\text{eff}}, \Delta R_{b_1\ell_1}, m_{hh}, \Delta R_{hh}, \cancel{E}_T$$

Here, $p_{T,2e2\mu}$ is the transverse momentum of the $2e2\mu$ system while the other variables have their usual meaning. The kinematic variables which discriminate between the signal and the backgrounds with maximal efficiency are: m_{bb} , ΔR_{bb} , $p_{T,bb}$ and m_{Z_2} . The normalized distribution of these four variables is illustrated in Fig. 12. The multivariate analysis using BDTD algorithm gives a signal significance of 0.77 and a S/B value of 0.12. The corresponding signal and background yields are listed in Table 8. Among the two different final states of $hh \rightarrow b\bar{b}ZZ^*$ considered in this work, the $2b4l'$ channel exhibits a slightly larger sensitivity compared to the $2b2e2\mu$ search channel. The signal and background yields from the XGBoost analysis are also listed in the same table. We obtain a slightly higher

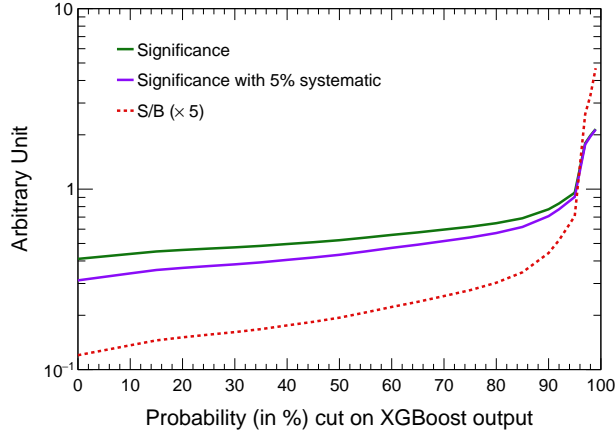


Figure 13: The variation of S/\sqrt{B} (with (5%) and without systematic uncertainty) and S/B is shown as a function of the probability cut on the XGBoost output for the $b\bar{b}ZZ^* \rightarrow b\bar{b} 2e2\mu$ channel.

signal significance (0.96) from the XGBoost analysis. Similar to the previous subsection, the probability cut on the XGBoost output has been applied at 95%. For the sake of completeness, we also show the variation of S/\sqrt{B} and S/B as a function of the probability cut in Fig. 13. The color code of Fig. 2 has been followed here.

	Process	Cross section order	Event yield after the analysis with	
			BDTD	XGBoost (probability cut > 95%)
Background	$t\bar{t}h$	NLO [147]	30	28
	$t\bar{t}Z$	NLO [155]	4.3	6.4
	Zh	NNLO (QCD) + NLO (EW) [147]	7.4	7.6
	Wh	NNLO (QCD) + NLO (EW) [147]	3×10^{-3}	3×10^{-3}
	Whc	LO	7×10^{-4}	9×10^{-4}
	$ggF-hb\bar{b}$	LO	2.7	3.5
	$ggF-hc\bar{c}$	LO	6×10^{-3}	8×10^{-3}
	$VBF-hjj$	NNLO (QCD) + NLO (EW) [147]	3×10^{-4}	4×10^{-4}
Total			44	45
Signal ($hh \rightarrow b\bar{b}ZZ^* \rightarrow 2b2e2\mu$)		NNLO [148]	5.1	6.4
Significance (S/\sqrt{B})			0.77	0.96

Table 8: The signal and background yields at the HE-LHC along with the signal significance for the $b\bar{b}ZZ^* \rightarrow 2b2e2\mu$ channel from the analysis using the BDTD and the XGBoost classifiers.

2.6 The $b\bar{b}\mu\mu$ channel

The di-Higgs final state often ignored in terms of clarity is the $b\bar{b}\mu\mu$ channel. The production rate of this channel is even lower than the $b\bar{b}\gamma\gamma$ final state due to the smaller branching ratio of $h \rightarrow \mu^+\mu^- \simeq 2.18 \times 10^{-4}$. The dominant background sources are: $t\bar{t}$ and the QCD-QED $b\bar{b}\mu\mu$. Sub-dominant contribution to the background comes from Zh , $t\bar{t}h$ and $b\bar{b}h$. Additionally, the fake backgrounds, *viz.* $c\bar{c}\mu\mu$ and $j\bar{j}\mu\mu$ also contribute when the c jets or the light jets get mistagged as b jets, respectively. We must mention that the $t\bar{t}$ background has been generated by decaying both the W bosons into the $\mu\nu_\mu$ pair. Contributions can also arise when the W bosons decay into the $\tau\nu_\tau$, however, we do not consider this contribution in our analysis due to its negligible rate. We also impose hard cuts at the generation level of the backgrounds and those have been listed in Appendix A.

Event selection demands exactly two b jets with $p_T > 30$ GeV and two isolated muons with $p_T > 20$ GeV. The final state b jets and the leptons are required to lie within $|\eta| < 4.0$. For consistency, we impose the generation level cuts: $\Delta R_{b_i\mu_j} > 0.2$ ($i, j = 1, 2$), $m_{\mu\mu} > 100$ GeV and $m_{bb} > 50$ GeV, at the selection level. The selected signal and background events are then subjected to a multivariate analysis using the BDTD algorithm and the XGBoost toolkit. The multivariate analysis is performed using the following kinematic variables:

$$p_{T,\mu\mu}, \Delta R_{\mu\mu}, m_{\mu\mu}, p_{T,bb}, \Delta R_{bb}, m_{bb}, H_T, p_{T,hh}, m_{hh}, \Delta R_{hh}, \cancel{E}_T,$$

where, H_T is the sum of the visible transverse momenta (sum of the p_T of the two b jets and the two final state muons) and all the variables have their usual meaning. The kinematic variables which are most effective in discriminating the signal from the backgrounds in the BDTD analysis are: m_{bb} , $m_{\mu\mu}$, \cancel{E}_T and $p_{T,\mu\mu}$. We illustrate the normalized distribution of these variables in Fig. 14. The signal and background yields along with the signal significance from the BDTD analysis have been listed in Table 9. Although, the $b\bar{b}\mu\mu$ channel offers a clean signal, it manifests a low value of signal significance due to huge contamination from the $t\bar{t}$ and $b\bar{b}\mu\mu$ backgrounds which are difficult to suppress. We also utilize XGBoost to discriminate the signal and the background events and perform a detailed collider analysis. The corresponding signal and background yields along with the signal significance are listed in Table 9. The XGBoost analysis results in a signal significance of 0.42 (with probability cut on XGBoost output at 97%) which is ~ 2 times the signal significance obtained from the BDTD analysis, but still remains short of being within the exclusion reach of HE-LHC. In Fig. 15, we show S/\sqrt{B} and S/B *vs.* probability cut on the XGBoost output following the color code from Fig. 2. At this point, we conclude our discussion on the future prospects of observing the non-resonant di-Higgs signature at the HE-LHC. In the next section, we study the ramifications of varying λ_h on the optimized

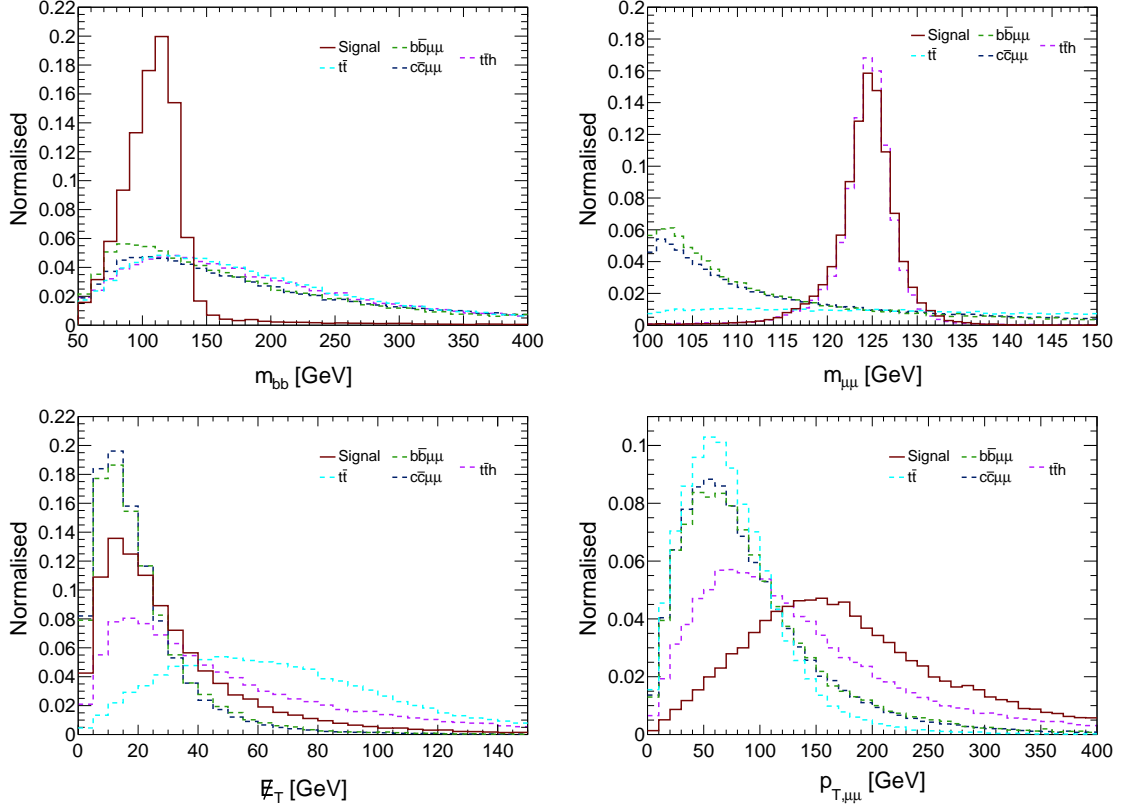


Figure 14: Normalized distributions of m_{bb} , $m_{\mu\mu}$, E_T and $p_{T,\mu\mu}$ for the $b\bar{b}\mu^+\mu^-$ signal and the dominant backgrounds after the acceptance cuts and the generation level cuts.

di-Higgs search strategies and the difference in the kinematics of the di-Higgs final states emerging from different values of λ_h .

	Process	Cross section order	Event yield after the analysis with	
			BDTD	XGBoost
Background	$t\bar{t} (\mu\mu)$	NNLO [154]	40799	24285
	$b\bar{b}\mu\mu$	LO	36963	11671
	$c\bar{c}\mu\mu$	LO	134	46
	$j\bar{j}\mu\mu$	LO	13	4.1
	Zh	NNLO (QCD) + NLO (EW) [147]	27	38
	$b\bar{b}h$	LO	0.95	2.2
	$t\bar{t}h$	NLO [147]	136	243
	Total		78074	36289
Signal ($hh \rightarrow b\bar{b}\mu\mu$)		NNLO [148]	58	80
Significance (S/\sqrt{B})			0.21	0.42

Table 9: The signal and background yields at the HE-LHC along with the signal significance for the $b\bar{b}\mu^+\mu^-$ channel from the analysis using the BDTD and the XGBoost classifiers.

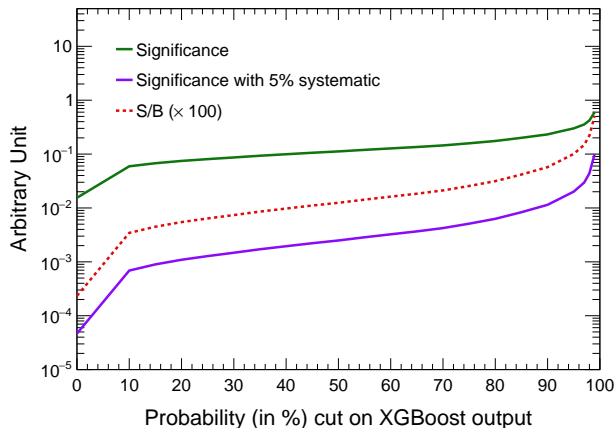


Figure 15: The variation of S/\sqrt{B} (with (5%) and without systematic uncertainty) and S/B is shown as a function of the probability cut on the XGBoost output for the $b\bar{b}\mu^+\mu^-$ channel.

3 Higgs self-coupling measurement

As discussed in Sec. 1, the LO di-Higgs production cross-section in the SM is an outcome of the destructive interference between the triangle (λ_h dependent) and the box diagrams. We must also note that the SM value of λ_h is a small number. Hence, the magnitude of interference between the two diagrams is highly sensitive to even small changes in λ_h . This strongly necessitates a detailed study of the implications of varying λ_h on the projected reach of non-resonant di-Higgs searches and the underlying changes in the kinematic distributions, which is precisely the goal of this section.

Before delving into the details of this section, we briefly summarize some of the existing results on the projected capability of constraining k_λ at the HL-LHC and the HE-LHC through direct and indirect measurements. The ATLAS detector is projected to be capable of constraining k_λ within $0.8 \leq k_\lambda \leq 7.7$ at 95% CL at the HL-LHC through a direct search of non-resonant di-Higgs production in the $b\bar{b}\gamma\gamma$ channel [92], while indirect probes of λ_h at the HL-LHC have projected an exclusion range of $0.1 \leq k_\lambda \leq 2.3$ at 68% CL [113]. The projected performance of the HE-LHC in constraining λ_h through a direct search in the $b\bar{b}\gamma\gamma$ channel has also been studied in Refs. [122, 128]. Ref. [128] and [122] have reported a projected sensitivity in the range of $0.6 \leq \lambda_h \leq 1.46$ at 1σ and $k_\lambda = 1 \pm 30\%$ at 95% CL, respectively. With these estimates in mind, and assuming a conservative approach, we study a wider range of k_λ and consider 7 different values of the same, *viz.* $k_\lambda = 4, 3, 2, 1, -0.5, -1$ and -2 .

k_λ	Signal cross-section (fb)	Efficiency		Signal yield		Background yield		S/\sqrt{B}	
		BDTD	XGBoost	BDTD	XGBoost	BDTD	XGBoost	BDTD	XGBoost
A. $pp \rightarrow hh \rightarrow b\bar{b}\gamma\gamma$									
−2	2.12	0.068	0.07	2162	2226	3410	1806	37	52.4
−1	1.35	0.076	0.078	1539	1579			26.4	37.2
−0.5	1.04	0.081	0.082	1264	1279			21.6	30.1
1	0.37	0.103	0.1	572	555			9.8	13.1
2	0.188	0.113	0.108	319	305			5.5	7.2
3	0.185	0.066	0.064	183	178			3.1	4.2
4	0.38	0.032	0.035	182	199			3.1	4.7
B. $pp \rightarrow hh \rightarrow b\bar{b}\tau\tau$									
−2	58.7	0.0045	0.004	3962	3522	155260	41795	10.1	17.2
−1	37.3	0.0052	0.0046	2912	2576			7.4	12.6
−0.5	28.7	0.0055	0.0047	2364	2020			6.0	9.9
1	10.2	0.0071	0.0064	1088	981			2.8	4.8
2	5.19	0.0077	0.0071	599	553			1.5	2.7
3	5.12	0.0047	0.0045	361	346			0.92	1.7
4	10.4	0.0023	0.0021	358	327			0.91	1.6
C. $pp \rightarrow hh \rightarrow b\bar{b}WW^*$									
−2	21.2	0.01	0.016	3183	5093	531600	365185	4.4	8.4
−1	13.5	0.0125	0.019	2531	3847			3.5	6.4
−0.5	10.4	0.013	0.021	2020	3263			2.8	5.4
1	3.69	0.02	0.03	1107	1661			1.5	2.7
2	1.87	0.026	0.037	729	1038			1	1.7
3	1.85	0.016	0.022	444	611			0.61	1.0
4	3.75	0.0062	0.009	349	506			0.48	0.84

Table 10: The cross-sections, signal efficiencies, signal yields, background yields, and the signal significances at the HE-LHC, obtained from the BDTD and the XGBoost analysis are listed along with the respective values of k_λ .

We generate the LO signal events for the new values of k_λ in the MG5_aMC@NLO framework by incorporating the UFO model file from [158]. We restrict our study of the Higgs self-coupling to the three most sensitive di-Higgs search channels from Sec. 2, *viz.* $b\bar{b}\gamma\gamma$, $b\bar{b}\tau^+\tau^-$ and $b\bar{b}WW^*$. The newly generated signal events corresponding to the different values of k_λ are passed through the BDTD and XGBoost frameworks which were optimized for the SM di-Higgs signal ($k_\lambda = 1$). The results for the $b\bar{b}\gamma\gamma$, $b\bar{b}\tau^+\tau^-$ and the $b\bar{b}WW^*$ channels are listed in Table 10. We have shown the production cross-section of the respective final states at different k_λ values along with the signal efficiency⁴ and the signal yields at the HE-LHC obtained from both, the BDTD and the XGBoost frameworks optimized for the SM hypothesis. The respective total background yields are also listed along with the signal significances computed assuming zero systematic uncertainties. Among the chosen values of k_λ , the non-resonant double Higgs production cross-section is the smallest for $k_\lambda = 3$, and continues to increase on its either side. The leading order squared amplitude for double

⁴Signal efficiency has been defined as the ratio of the number of signal events which pass the respective analysis frameworks to the total number of generated event samples.

Higgs production can be factorized into three different contributions: the triangle diagram ($\propto \lambda_h^2$), box diagram (independent of λ_h) and the interference between these two diagrams ($\propto \lambda_h$). For positive values of λ_h , the interference term contributes negatively, resulting in a destructive interference between the box and triangle diagrams [159]. Therefore, as we increase the values of k_λ away from the SM hypothesis, we initially observe a reduction in the di-Higgs production rate due to a larger destructive interference, *viz.* $k_\lambda = 2, 3$. Upon moving to an even larger value of λ_h ($k_\lambda = 4$), the contributions from the triangle loop which are proportional to λ_h squared, starts compensating the reduction from the negative interference term resulting in an increase in the di-Higgs production rate. As we move towards the negative values of k_λ , a dramatic increase is observed in the di-Higgs cross-section since the interference term begins to contribute constructively.

In all the di-Higgs search channels considered in this section, we observe a roughly uniform trend in the variation of signal efficiency as a function of k_λ . Both, the BDTD and the XGBoost classifiers (both trained for the SM hypothesis), exhibit the highest signal efficiency for $k_\lambda = 2$ with a gradual decrease towards higher as well as smaller values of k_λ . For example, in the case of $b\bar{b}\gamma\gamma$ channel, the BDTD (XGBoost) optimization result in a signal efficiency of 0.068 (0.07), 0.103 (0.1), 0.113 (0.108) and 0.032 (0.035) at $k_\lambda = -2, 1, 2$ and 4, respectively. We would like to clarify again that we have not performed the signal significance optimization for the respective k_λ signals, and have used the BDTD and the XGBoost classifiers optimized for the case of $k_\lambda = 1$. The signals corresponding to the different values of k_λ have been simply passed through the classifiers optimized for the case of $k_\lambda = 1$. We must note that even with the classifiers optimized for the case of $k_\lambda = 1$, the signal efficiency is highest for $k_\lambda = 2$. This occurs despite the $k_\lambda = 2$ signal having a relatively smaller cross-section compared to most of its counterparts. In order to attain a better viewpoint, we illustrate the normalized distribution of the probability of new physics signal events corresponding to the different values of k_λ to look like the respective SM di-Higgs signal ($k_\lambda = 1$) in the left panel of Fig. 16. The probability distribution of the NP signals to look like the respective dominant SM backgrounds: QCD-QED $b\bar{b}\gamma\gamma$ (for the $b\bar{b}\gamma\gamma$ channel), $b\bar{b}jj$ (for the $b\bar{b}\tau^+\tau^-$ channel) and $t\bar{t}$ (for the $b\bar{b}WW^*$ channel), respectively, is illustrated in the right panels of Fig. 16. The XGBoost toolkit was used to derive these probability distributions. It can be observed from the distributions in the left panel of Fig. 16 that the $k_\lambda = 2$ scenario (shown in red color) has the largest number of events in the highest probability bin for all three signal channels. The k_λ signals in decreasing order of signal efficiency at the highest probability bin can be noted from the left panels in Fig. 16 to be: $k_\lambda = 2$ (highest), 1 (green color), -0.5 (orange color), -2 (blue color) and 4 (purple color). This sequence holds true for all the three di-Higgs final states considered in the present section. It must be noted that the above mentioned ordering also stands at the lowest probability bin in the background-like probability distribution of the k_λ signals (right panel of Fig. 16). Furthermore, in the lower right panel of Fig. 16, where

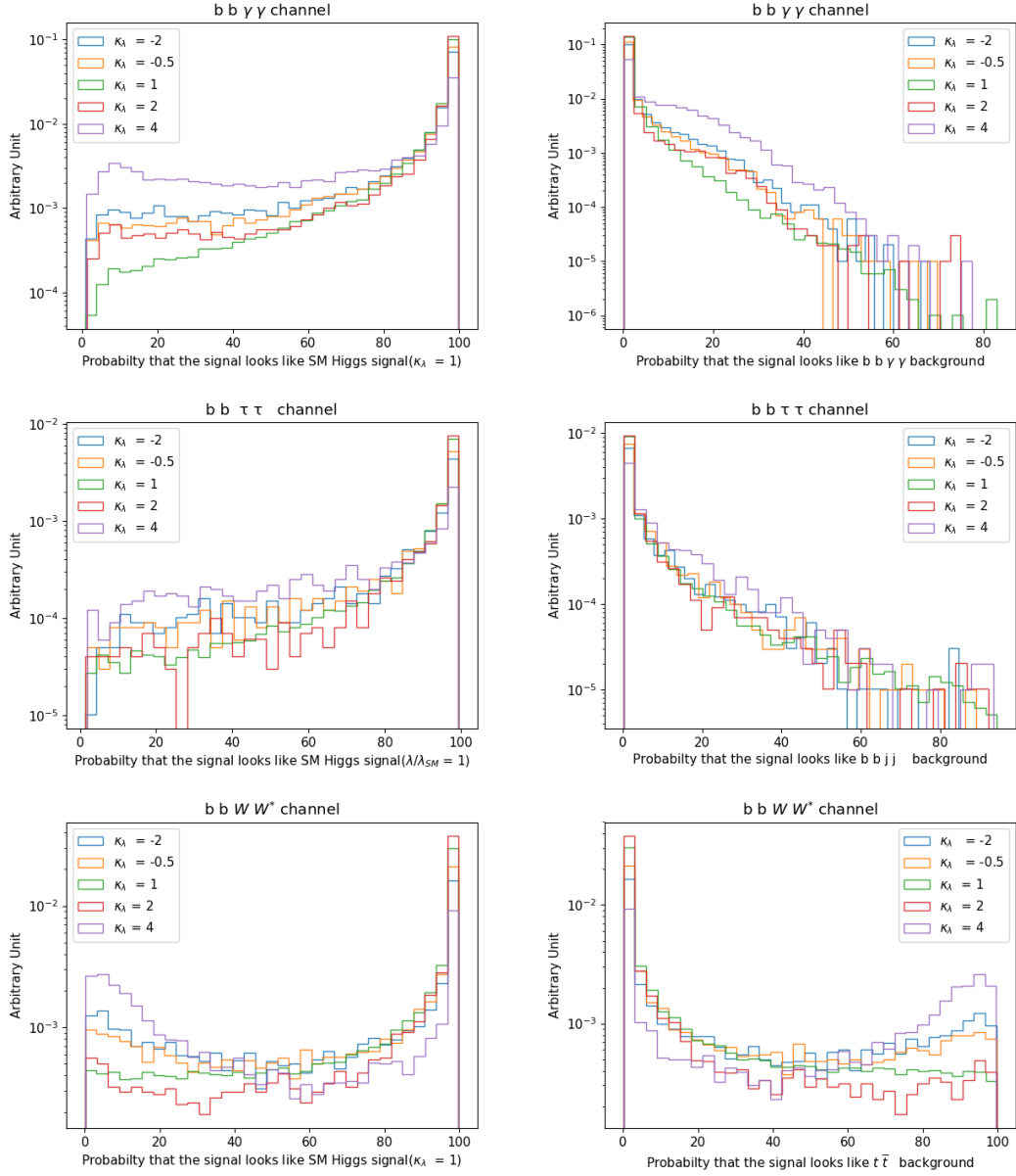


Figure 16: Normalized distributions illustrating the probability that the signal events in the $b\bar{b}\gamma\gamma$ (top), $b\bar{b}\tau\tau$ (center) and $b\bar{b}WW^*$ (bottom) channel look like the respective SM di-Higgs signal (shown in the left panels) and respective dominant SM backgrounds (shown in the right panels).

we illustrate the normalized distribution of the probability that the various k_λ signals in the fully-leptonic $b\bar{b}WW^*$ channel look like the dominant $t\bar{t}$ background, we observe a second peak towards the higher end. This indicates that the $b\bar{b}WW^*$ signal corresponding to $k_\lambda = 4$ (purple color), $k_\lambda = 2$ (cyan color) and $k_\lambda = -0.5$ (orange color), also has a relatively high probability to resemble the dominant $t\bar{t}$ background, making the signal-

background discrimination more challenging. This trend is also reflected in the low signal efficiency for these k_λ signals.

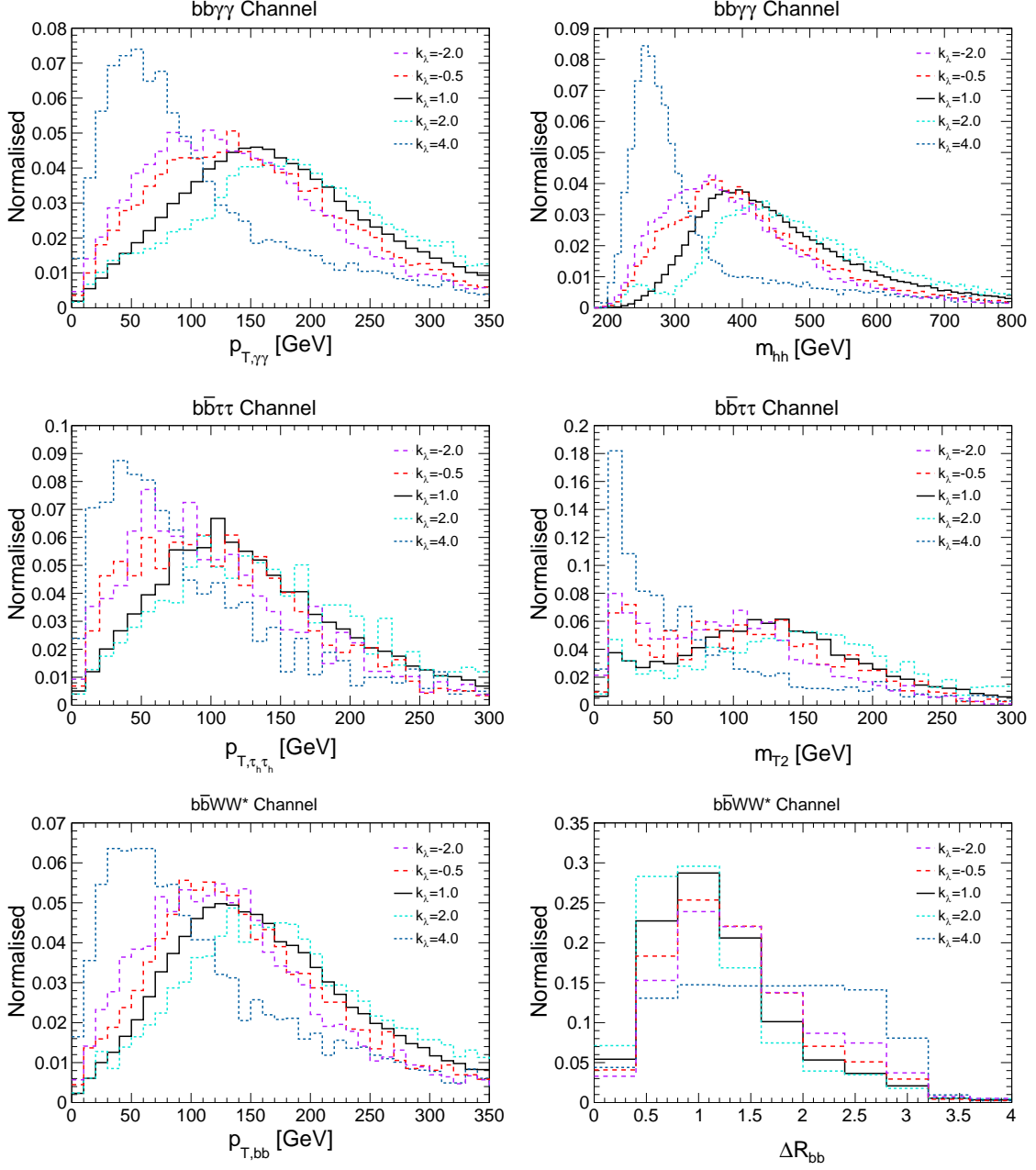


Figure 17: Normalized distribution of (a) $p_{T,\gamma\gamma}$ and m_{hh} in the $b\bar{b}\gamma\gamma$ channel (top), (b) $p_{T,\tau_h\tau_h}$ and m_{T2} in the $b\bar{b}\tau\tau$ channel (middle), (c) $p_{T,bb}$ and ΔR_{bb} in the $b\bar{b}WW^*$ channel (bottom), for different values of $k_\lambda = \lambda/\lambda_{SM}$.

As discussed earlier, varying k_λ also leads to modified kinematic distributions. In Fig. 17, we illustrate the difference in kinematic distributions arising from different values

of the Higgs self-coupling. In the top panel of Fig. 17, we show the normalized distribution of $p_{T,\gamma\gamma}$ (left) and m_{hh} (right) in the $b\bar{b}\gamma\gamma$ channel for $k_\lambda = -2, -0.5, 1, 2$ and 4 . In the central (bottom) panels of Fig. 17, we illustrate the normalized distribution of $p_{T,\tau_h\tau_h}$ (left-side) and m_{T2} (right-side) ($p_{T,bb}$ (left-side) and ΔR_{bb} (right-side)) for the $b\bar{b}\tau^+\tau^-$ ($b\bar{b}WW^*$) channel. Among the p_T distributions illustrated in the left panel of Fig. 17, we see that the distribution for $k_\lambda = 4$ stands out in all three channels with a peak at relatively smaller values compared to their other counterparts. The reason behind this observation is the increased contribution from the triangle diagram. We see a roughly similar behavior in the m_{T2} and m_{hh} distributions. In the lower right panel of Fig. 17, we observe that the ΔR_{bb} distribution for $k_\lambda = 4$ signal becomes flatter compared to the other signals due to relatively smaller p_T of the parent Higgs boson.

The results from this section strongly indicate that the SM di-Higgs search analyses can be very sensitive to new physics effects arising from a different value of the yet unmeasured Higgs self-coupling. It is therefore of utmost importance to have an understanding of the differences in the kinematic properties emerging from varying λ_h while searching for new physics as well as the double Higgs production at the futuristic HE-LHC. We would also like to emphasize that the HE-LHC will be sensitive to the entire range of k_λ considered in this section through non-resonant di-Higgs searches. The signal significances listed in Table 10 show that the combination of search results in the $b\bar{b}\gamma\gamma$, $b\bar{b}\tau^+\tau^-$ and $b\bar{b}W^+W^-$ channels would result in a combined signal significance of 4.6σ at the HE-LHC for the $k_\lambda = 3$ scenario. Combination of search results in the same three channels for the $k_\lambda = 2$ and 4 scenarios result in a projected signal significance of $> 5\sigma$ at the HE-LHC. The smaller values of k_λ , *viz.* $k_\lambda = -0.5, -1$ and -2 , result in an impressive projected signal significance of $> 30\sigma$, while the SM hypothesis also exhibits a projected signal significance of $> 10\sigma$. We conclude this section by highlighting upon the need to improve the discrimination capability between the modifications arising from a variation in λ_h to constrain the Higgs self-coupling more precisely.

4 Summary

In the first part of this work, we studied the future potential of the HE-LHC in probing the non-resonant double Higgs production in the SM in several final states by performing multivariate analysis using the BDTD algorithm, the XGBoost toolkit and DNN. In this regard, we analyzed the $b\bar{b}\gamma\gamma$, fully hadronic $b\bar{b}\tau\tau$, fully leptonic $b\bar{b}WW^*$, fully leptonic $WW^*\gamma\gamma$, the $2b4l'$ and $2b2e2\mu$ final states of $b\bar{b}ZZ^*$, and, the $b\bar{b}\mu\mu$ channels. The highest signal significance and S/B value was observed in the $b\bar{b}\gamma\gamma$ channel, where we obtained a signal significance of 9.8, 13.1 and 10.4, from the BDTD, XGBoost and DNN classifiers, respectively. The $b\bar{b}\gamma\gamma$ channel, thus, displays a discovery potential at the HE-LHC. The second most promising search channel was observed to be the $b\bar{b}\tau^+\tau^-$ final state with

a signal significance of 2.8 (BDTD), 4.8 (XGBoost) and 4.3 (DNN). The fully leptonic $b\bar{b}WW^*$ channel was also analyzed using these three classifiers and a signal significance of 1.5, 2.7 and 1.4 was observed from the analysis using BDTD, XGBoost and DNN. In the aforesaid channels, the performance of the XGBoost classifier was better than the BDTD and DNN. The XGBoost toolkit resulted in a signal significance which was higher than its BDTD counterpart by $\sim 35\%$, $\sim 80\%$ and $\sim 80\%$ in the $b\bar{b}\gamma\gamma$, $b\bar{b}\tau^+\tau^-$ and $b\bar{b}WW^*$ channels, respectively. We also analyzed the $WW^*\gamma\gamma$, $b\bar{b}ZZ^*$ and the $b\bar{b}\mu^+\mu^-$ search channels using the BDTD and the XGBoost classifiers. We obtained a signal significance of 1.7 (BDTD) and 2.1 (XGBoost) in the $WW^*\gamma\gamma$ channel and the second highest S/B value after the $b\bar{b}\gamma\gamma$ channel. The $2b4l'$ and the $2b2e2\mu$ final states arising from $b\bar{b}ZZ^*$ were also subjected to the BDTD and XGBoost optimizations, and both of these final states resulted in a signal significance of $< 1\sigma$. However, combining the XGBoost search results for these two final states result in a signal significance of 1.8. The $b\bar{b}ZZ^*$ mode also exhibited an impressive S/B value. The future potential of the $b\bar{b}\mu^+\mu^-$ channel at the HE-LHC was also analyzed, and we obtained a signal significance of 0.21 and 0.42 using the BDTD and the XGBoost classifiers, respectively. Combination of results from all the search channels considered in this work yield a combined projected signal significance of 10.5 and 14.4 from the BDTD and the XGBoost classifiers, respectively. These projections indicate towards the possibility to observe the non-resonant di-Higgs signal at the HE-LHC at discovery potential.

In the second part, the implications of varying k_λ on the potential reach of the $b\bar{b}\gamma\gamma$, $b\bar{b}\tau^+\tau^-$ and $b\bar{b}WW^*$ search analyses optimized for the SM hypothesis is studied along with the variations in the kinematics of the di-Higgs final states emerging from varying k_λ . In this respect, we consider the following values of k_λ : -2, -1, -0.5, 1, 2, 3 and 4. The signal events corresponding to these different values of k_λ were passed through the BDTD and XGBoost classifiers trained for the case of $k_\lambda = 1$. Both, the BDTD and the XGBoost classifiers, exhibit a signal significance of $> 5\sigma$ for $k_\lambda = -2, -1, -0.5, 1$ and 2, and a signal significance of $> 2\sigma$ for $k_\lambda = 3$ and 4. Combination of searches in the $b\bar{b}\gamma\gamma$, $b\bar{b}\tau^+\tau^-$ and $b\bar{b}WW^*$ channels result in a signal significance of $> 5\sigma$ even for the $k_\lambda = 4$ scenario. Our projections thus indicate that the HE-LHC would be sensitive to the entire range of k_λ considered in this work through direct searches in the non-resonant di-Higgs search channels.

Acknowledgments

The authors thank Shankha Banerjee for the helpful discussions on this work. The work of BB is supported by the Department of Science and Technology, Government of India, under the Grant Agreement number IFA13-PH-75 (INSPIRE Faculty Award).

References

- [1] ATLAS collaboration, G. Aad et al., *Observation of a new particle in the search for the Standard Model Higgs boson with the ATLAS detector at the LHC*, *Phys. Lett. B* **716** (2012) 1–29, [[1207.7214](#)].
- [2] CMS collaboration, S. Chatrchyan et al., *Observation of a new boson at a mass of 125 GeV with the CMS experiment at the LHC*, *Phys. Lett. B* **716** (2012) 30–61, [[1207.7235](#)].
- [3] CMS collaboration, A. M. Sirunyan et al., *Combined measurements of Higgs boson couplings in proton-proton collisions at $\sqrt{s} = 13$ TeV*, *Submitted to: Eur. Phys. J.* (2018) , [[1809.10733](#)].
- [4] ATLAS collaboration, M. Aaboud et al., *Search for Higgs bosons produced via vector-boson fusion and decaying into bottom quark pairs in $\sqrt{s} = 13$ TeV pp collisions with the ATLAS detector*, *Phys. Rev. D* **98** (2018) 052003, [[1807.08639](#)].
- [5] ATLAS collaboration, M. Aaboud et al., *Observation of $H \rightarrow b\bar{b}$ decays and VH production with the ATLAS detector*, *Phys. Lett. B* **786** (2018) 59–86, [[1808.08238](#)].
- [6] ATLAS collaboration, M. Aaboud et al., *Evidence for the associated production of the Higgs boson and a top quark pair with the ATLAS detector*, *Phys. Rev. D* **97** (2018) 072003, [[1712.08891](#)].
- [7] ATLAS collaboration, M. Aaboud et al., *Measurements of gluon-gluon fusion and vector-boson fusion Higgs boson production cross-sections in the $H \rightarrow WW^* \rightarrow e\nu\mu\nu$ decay channel in pp collisions at $\sqrt{s} = 13$ TeV with the ATLAS detector*, *Phys. Lett. B* **789** (2019) 508–529, [[1808.09054](#)].
- [8] ATLAS collaboration, M. Aaboud et al., *Measurements of Higgs boson properties in the diphoton decay channel with 36 fb^{-1} of pp collision data at $\sqrt{s} = 13$ TeV with the ATLAS detector*, *Phys. Rev. D* **98** (2018) 052005, [[1802.04146](#)].
- [9] CMS collaboration, A. M. Sirunyan et al., *Observation of Higgs boson decay to bottom quarks*, *Phys. Rev. Lett.* **121** (2018) 121801, [[1808.08242](#)].
- [10] CMS collaboration, A. M. Sirunyan et al., *Measurements of the Higgs boson width and anomalous HVV couplings from on-shell and off-shell production in the four-lepton final state*, *Phys. Rev. D* **99** (2019) 112003, [[1901.00174](#)].
- [11] M. Grazzini, G. Heinrich, S. Jones, S. Kallweit, M. Kerner, J. M. Lindert et al., *Higgs boson pair production at NNLO with top quark mass effects*, *JHEP* **05** (2018) 059, [[1803.02463](#)].
- [12] J. Baglio, O. Eberhardt, U. Nierste and M. Wiebusch, *Benchmarks for Higgs Pair Production and Heavy Higgs boson Searches in the Two-Higgs-Doublet Model of Type II*, *Phys. Rev. D* **90** (2014) 015008, [[1403.1264](#)].
- [13] B. Hespel, D. Lopez-Val and E. Vryonidou, *Higgs pair production via gluon fusion in the Two-Higgs-Doublet Model*, *JHEP* **09** (2014) 124, [[1407.0281](#)].
- [14] L.-C. Lü, C. Du, Y. Fang, H.-J. He and H. Zhang, *Searching heavier Higgs boson via di-Higgs production at LHC Run-2*, *Phys. Lett. B* **755** (2016) 509–522, [[1507.02644](#)].

- [15] L. Bian and N. Chen, *Higgs pair productions in the CP-violating two-Higgs-doublet model*, *JHEP* **09** (2016) 069, [[1607.02703](#)].
- [16] G. D. Kribs and A. Martin, *Enhanced di-Higgs Production through Light Colored Scalars*, *Phys. Rev.* **D86** (2012) 095023, [[1207.4496](#)].
- [17] S. Dawson, E. Furlan and I. Lewis, *Unravelling an extended quark sector through multiple Higgs production?*, *Phys. Rev.* **D87** (2013) 014007, [[1210.6663](#)].
- [18] A. Pierce, J. Thaler and L.-T. Wang, *Disentangling Dimension Six Operators through Di-Higgs Boson Production*, *JHEP* **05** (2007) 070, [[hep-ph/0609049](#)].
- [19] S. Kanemura and K. Tsumura, *Effects of the anomalous Higgs couplings on the Higgs boson production at the Large Hadron Collider*, *Eur. Phys. J.* **C63** (2009) 11–21, [[0810.0433](#)].
- [20] K. Nishiwaki, S. Niyogi and A. Shivaji, *ttH Anomalous Coupling in Double Higgs Production*, *JHEP* **04** (2014) 011, [[1309.6907](#)].
- [21] U. Ellwanger, *Higgs pair production in the NMSSM at the LHC*, *JHEP* **08** (2013) 077, [[1306.5541](#)].
- [22] C.-R. Chen and I. Low, *Double take on new physics in double Higgs boson production*, *Phys. Rev.* **D90** (2014) 013018, [[1405.7040](#)].
- [23] N. Liu, S. Hu, B. Yang and J. Han, *Impact of top-Higgs couplings on Di-Higgs production at future colliders*, *JHEP* **01** (2015) 008, [[1408.4191](#)].
- [24] M. Slawinska, W. van den Wollenberg, B. van Eijk and S. Bentvelsen, *Phenomenology of the trilinear Higgs coupling at proton-proton colliders*, [1408.5010](#).
- [25] F. Goertz, A. Papaefstathiou, L. L. Yang and J. Zurita, *Higgs boson pair production in the $D=6$ extension of the SM*, *JHEP* **04** (2015) 167, [[1410.3471](#)].
- [26] A. Azatov, R. Contino, G. Panico and M. Son, *Effective field theory analysis of double Higgs boson production via gluon fusion*, *Phys. Rev.* **D92** (2015) 035001, [[1502.00539](#)].
- [27] C.-T. Lu, J. Chang, K. Cheung and J. S. Lee, *An exploratory study of Higgs-boson pair production*, *JHEP* **08** (2015) 133, [[1505.00957](#)].
- [28] A. Carvalho, M. Dall’Osso, T. Dorigo, F. Goertz, C. A. Gottardo and M. Tosi, *Higgs Pair Production: Choosing Benchmarks With Cluster Analysis*, *JHEP* **04** (2016) 126, [[1507.02245](#)].
- [29] M. Gorbahn and U. Haisch, *Indirect probes of the trilinear Higgs coupling: $gg \rightarrow h$ and $h \rightarrow \gamma\gamma$* , *JHEP* **10** (2016) 094, [[1607.03773](#)].
- [30] A. Carvalho, M. Dall’Osso, P. De Castro Manzano, T. Dorigo, F. Goertz, M. Gouzevich et al., *Analytical parametrization and shape classification of anomalous HH production in the EFT approach*, [1608.06578](#).
- [31] S. Banerjee, B. Batell and M. Spannowsky, *Invisible decays in Higgs boson pair production*, *Phys. Rev.* **D95** (2017) 035009, [[1608.08601](#)].
- [32] Q.-H. Cao, G. Li, B. Yan, D.-M. Zhang and H. Zhang, *Double Higgs production at the 14 TeV LHC and the 100 TeV pp -collider*, [1611.09336](#).

- [33] M. J. Dolan, C. Englert and M. Spannowsky, *New Physics in LHC Higgs boson pair production*, *Phys. Rev.* **D87** (2013) 055002, [[1210.8166](#)].
- [34] R. Contino, C. Grojean, M. Moretti, F. Piccinini and R. Rattazzi, *Strong Double Higgs Production at the LHC*, *JHEP* **05** (2010) 089, [[1002.1011](#)].
- [35] R. Grober and M. Muhlleitner, *Composite Higgs Boson Pair Production at the LHC*, *JHEP* **06** (2011) 020, [[1012.1562](#)].
- [36] R. Contino, M. Ghezzi, M. Moretti, G. Panico, F. Piccinini and A. Wulzer, *Anomalous Couplings in Double Higgs Production*, *JHEP* **08** (2012) 154, [[1205.5444](#)].
- [37] R. Grober, M. Muhlleitner and M. Spira, *Signs of Composite Higgs Pair Production at Next-to-Leading Order*, *JHEP* **06** (2016) 080, [[1602.05851](#)].
- [38] J.-J. Liu, W.-G. Ma, G. Li, R.-Y. Zhang and H.-S. Hou, *Higgs boson pair production in the little Higgs model at hadron collider*, *Phys. Rev.* **D70** (2004) 015001, [[hep-ph/0404171](#)].
- [39] C. O. Dib, R. Rosenfeld and A. Zerwekh, *Double Higgs production and quadratic divergence cancellation in little Higgs models with T parity*, *JHEP* **05** (2006) 074, [[hep-ph/0509179](#)].
- [40] L. Wang, W. Wang, J. M. Yang and H. Zhang, *Higgs-pair production in littlest Higgs model with T -parity*, *Phys. Rev.* **D76** (2007) 017702, [[0705.3392](#)].
- [41] V. Barger, L. L. Everett, C. B. Jackson, A. D. Peterson and G. Shaughnessy, *New physics in resonant production of Higgs boson pairs*, *Phys. Rev. Lett.* **114** (2015) 011801, [[1408.0003](#)].
- [42] K. Nakamura, K. Nishiwaki, K.-y. Oda, S. C. Park and Y. Yamamoto, *Di-higgs enhancement by neutral scalar as probe of new colored sector*, *Eur. Phys. J. C* **77** (2017) 273, [[1701.06137](#)].
- [43] A. Crivellin, M. Ghezzi and M. Procura, *Effective Field Theory with Two Higgs Doublets*, *JHEP* **09** (2016) 160, [[1608.00975](#)].
- [44] J. Cao, Z. Heng, L. Shang, P. Wan and J. M. Yang, *Pair Production of a 125 GeV Higgs Boson in MSSM and NMSSM at the LHC*, *JHEP* **04** (2013) 134, [[1301.6437](#)].
- [45] H. Sun, Y.-J. Zhou and H. Chen, *Constraints on large-extra-dimensions model through 125-GeV Higgs pair production at the LHC*, *Eur. Phys. J. C* **72** (2012) 2011, [[1211.5197](#)].
- [46] R. Costa, M. Muhlleitner, M. O. P. Sampaio and R. Santos, *Singlet Extensions of the Standard Model at LHC Run 2: Benchmarks and Comparison with the NMSSM*, *JHEP* **06** (2016) 034, [[1512.05355](#)].
- [47] J. M. No and M. Ramsey-Musolf, *Probing the Higgs Portal at the LHC Through Resonant di-Higgs Production*, *Phys. Rev.* **D89** (2014) 095031, [[1310.6035](#)].
- [48] A. V. Kotwal, M. J. Ramsey-Musolf, J. M. No and P. Winslow, *Singlet-catalyzed electroweak phase transitions in the 100 TeV frontier*, *Phys. Rev.* **D94** (2016) 035022, [[1605.06123](#)].
- [49] Y. Gao and N. A. Neill, *Probing Exotic Triple Higgs Couplings for Almost Inert Higgs Bosons at the LHC*, *JHEP* **05** (2020) 087, [[2001.00069](#)].
- [50] K. Cheung, A. Jueid, C.-T. Lu, J. Song and Y. W. Yoon, *Disentangling new physics effects on non-resonant Higgs boson pair production from gluon fusion*, [2003.11043](#).

- [51] P. Huang and Y. H. Ng, *Di-Higgs Production in SUSY models at the LHC*, [1910.13968](#).
- [52] D. Barducci, K. Mimasu, J. No, C. Vernieri and J. Zurita, *Enlarging the scope of resonant di-Higgs searches: Hunting for Higgs-to-Higgs cascades in 4b final states at the LHC and future colliders*, *JHEP* **02** (2020) 002, [[1910.08574](#)].
- [53] P. Basler, S. Dawson, C. Englert and M. Mühlleitner, *Di-Higgs boson peaks and top valleys: Interference effects in Higgs sector extensions*, *Phys. Rev. D* **101** (2020) 015019, [[1909.09987](#)].
- [54] A. Alves, D. Gonçalves, T. Ghosh, H.-K. Guo and K. Sinha, *Di-Higgs Production in the 4b Channel and Gravitational Wave Complementarity*, *JHEP* **03** (2020) 053, [[1909.05268](#)].
- [55] C. Englert and J. Jaeckel, *Probing the Symmetric Higgs Portal with Di-Higgs Boson Production*, *Phys. Rev. D* **100** (2019) 095017, [[1908.10615](#)].
- [56] K. Babu and S. Jana, *Enhanced Di-Higgs Production in the Two Higgs Doublet Model*, *JHEP* **02** (2019) 193, [[1812.11943](#)].
- [57] P. Basler, S. Dawson, C. Englert and M. Mühlleitner, *Showcasing HH production: Benchmarks for the LHC and HL-LHC*, *Phys. Rev. D* **99** (2019) 055048, [[1812.03542](#)].
- [58] M. Bauer, M. Carena and A. Carmona, *Higgs Pair Production as a Signal of Enhanced Yukawa Couplings*, *Phys. Rev. Lett.* **121** (2018) 021801, [[1801.00363](#)].
- [59] M. Flores, C. Gross, J. S. Kim, O. Lebedev and S. Mondal, *Multi-Higgs Probes of the Dark Sector*, [1912.02204](#).
- [60] C. Englert, D. J. Miller and D. D. Smaranda, *Phenomenology of GUT-inspired gauge-Higgs unification*, [1911.05527](#).
- [61] J. Alison et al., *Higgs Boson Pair Production at Colliders: Status and Perspectives*, in *Double Higgs Production at Colliders* (B. Di Micco, M. Gouzevitch, J. Mazzitelli and C. Vernieri, eds.), 9, 2019. [1910.00012](#).
- [62] L. Alasfar, R. Corral Lopez and R. Gröber, *Probing Higgs couplings to light quarks via Higgs pair production*, *JHEP* **11** (2019) 088, [[1909.05279](#)].
- [63] M. Capozzi and G. Heinrich, *Exploring anomalous couplings in Higgs boson pair production through shape analysis*, *JHEP* **03** (2020) 091, [[1908.08923](#)].
- [64] G. Li, L.-X. Xu, B. Yan and C.-P. Yuan, *Resolving the degeneracy in top quark Yukawa coupling with Higgs pair production*, *Phys. Lett. B* **800** (2020) 135070, [[1904.12006](#)].
- [65] A. Alves, T. Ghosh, H.-K. Guo, K. Sinha and D. Vagie, *Collider and Gravitational Wave Complementarity in Exploring the Singlet Extension of the Standard Model*, *JHEP* **04** (2019) 052, [[1812.09333](#)].
- [66] A. Adhikary, S. Banerjee, R. Kumar Barman and B. Bhattacharjee, *Resonant heavy Higgs searches at the HL-LHC*, *JHEP* **09** (2019) 068, [[1812.05640](#)].
- [67] S. Borowka, C. Duhr, F. Maltoni, D. Pagani, A. Shivaji and X. Zhao, *Probing the scalar potential via double Higgs boson production at hadron colliders*, *JHEP* **04** (2019) 016, [[1811.12366](#)].

- [68] N. Chen, C. Du, Y. Wu and X.-J. Xu, *Further study of the global minimum constraint on the two-Higgs-doublet models: LHC searches for heavy Higgs bosons*, *Phys. Rev. D* **99** (2019) 035011, [[1810.04689](#)].
- [69] A. Alves, T. Ghosh, H.-K. Guo and K. Sinha, *Resonant Di-Higgs Production at Gravitational Wave Benchmarks: A Collider Study using Machine Learning*, *JHEP* **12** (2018) 070, [[1808.08974](#)].
- [70] G. Buchalla, M. Capozzi, A. Celis, G. Heinrich and L. Scyboz, *Higgs boson pair production in non-linear Effective Field Theory with full m_t -dependence at NLO QCD*, *JHEP* **09** (2018) 057, [[1806.05162](#)].
- [71] Z. Heng, X. Gong and H. Zhou, *Pair production of Higgs boson in NMSSM at the LHC with the next-to-lightest CP-even Higgs boson being SM-like*, *Chin. Phys. C* **42** (2018) 073103, [[1805.01598](#)].
- [72] J. H. Kim, Y. Sakaki and M. Son, *Combined analysis of double Higgs production via gluon fusion at the HL-LHC in the effective field theory approach*, *Phys. Rev. D* **98** (2018) 015016, [[1801.06093](#)].
- [73] ATLAS collaboration, G. Aad et al., *Combination of searches for Higgs boson pairs in pp collisions at $\sqrt{s}=13$ TeV with the ATLAS detector*, *Phys. Lett. B* **800** (2020) 135103, [[1906.02025](#)].
- [74] ATLAS collaboration, M. Aaboud et al., *Search for Higgs boson pair production in the $WW^{(*)}WW^{(*)}$ decay channel using ATLAS data recorded at $\sqrt{s}=13$ TeV*, *JHEP* **05** (2019) 124, [[1811.11028](#)].
- [75] ATLAS collaboration, M. Aaboud et al., *Search for Higgs boson pair production in the $b\bar{b}WW^*$ decay mode at $\sqrt{s}=13$ TeV with the ATLAS detector*, *JHEP* **04** (2019) 092, [[1811.04671](#)].
- [76] ATLAS collaboration, M. Aaboud et al., *Search for resonant and non-resonant Higgs boson pair production in the $b\bar{b}\tau^+\tau^-$ decay channel in pp collisions at $\sqrt{s}=13$ TeV with the ATLAS detector*, *Phys. Rev. Lett.* **121** (2018) 191801, [[1808.00336](#)].
- [77] CMS collaboration, A. M. Sirunyan et al., *Search for Higgs boson pair production in events with two bottom quarks and two tau leptons in proton-proton collisions at $\sqrt{s}=13$ TeV*, *Phys. Lett. B* **778** (2018) 101–127, [[1707.02909](#)].
- [78] ATLAS collaboration, M. Aaboud et al., *Search for Higgs boson pair production in the $\gamma\gamma WW^*$ channel using pp collision data recorded at $\sqrt{s}=13$ TeV with the ATLAS detector*, *Eur. Phys. J. C* **78** (2018) 1007, [[1807.08567](#)].
- [79] ATLAS collaboration, M. Aaboud et al., *Search for Higgs boson pair production in the $\gamma\gamma b\bar{b}$ final state with 13 TeV pp collision data collected by the ATLAS experiment*, *JHEP* **11** (2018) 040, [[1807.04873](#)].
- [80] CMS collaboration, *Search for Higgs boson pair production in the final state containing two photons and two bottom quarks in proton-proton collisions at $\sqrt{s}=13$ TeV*, .
- [81] ATLAS collaboration, M. Aaboud et al., *Search for pair production of Higgs bosons in the*

- $b\bar{b}b\bar{b}$ final state using proton-proton collisions at $\sqrt{s} = 13$ TeV with the ATLAS detector, *JHEP* **01** (2019) 030, [[1804.06174](#)].
- [82] ATLAS collaboration, G. Aad et al., *Search for non-resonant Higgs boson pair production in the $b\bar{b}l\nu l\nu$ final state with the ATLAS detector in pp collisions at $\sqrt{s} = 13$ TeV*, *Phys. Lett. B* **801** (2020) 135145, [[1908.06765](#)].
- [83] CMS collaboration, A. M. Sirunyan et al., *Search for resonant and nonresonant Higgs boson pair production in the $b\bar{b}l\nu l\nu$ final state in proton-proton collisions at $\sqrt{s} = 13$ TeV*, *JHEP* **01** (2018) 054, [[1708.04188](#)].
- [84] CMS collaboration, A. M. Sirunyan et al., *Combination of searches for Higgs boson pair production in proton-proton collisions at $\sqrt{s} = 13$ TeV*, *Phys. Rev. Lett.* **122** (2019) 121803, [[1811.09689](#)].
- [85] CMS collaboration, *Search for non-resonant pair production of Higgs bosons in the $b\bar{b}b\bar{b}$ final state with 13 TeV CMS data*, .
- [86] ATLAS collaboration, G. Aad et al., *Search For Higgs Boson Pair Production in the $\gamma\gamma b\bar{b}$ Final State using pp Collision Data at $\sqrt{s} = 8$ TeV from the ATLAS Detector*, *Phys. Rev. Lett.* **114** (2015) 081802, [[1406.5053](#)].
- [87] ATLAS collaboration, G. Aad et al., *Search for Higgs boson pair production in the $b\bar{b}b\bar{b}$ final state from pp collisions at $\sqrt{s} = 8$ TeV with the ATLAS detector*, *Eur. Phys. J. C* **75** (2015) 412, [[1506.00285](#)].
- [88] ATLAS collaboration, G. Aad et al., *Searches for Higgs boson pair production in the $hh \rightarrow b\bar{b}\tau\tau, \gamma\gamma WW^*, \gamma\gamma b\bar{b}, b\bar{b}b\bar{b}$ channels with the ATLAS detector*, *Phys. Rev.* **D92** (2015) 092004, [[1509.04670](#)].
- [89] ATLAS collaboration, M. Aaboud et al., *Search for pair production of Higgs bosons in the $b\bar{b}b\bar{b}$ final state using proton-proton collisions at $\sqrt{s} = 13$ TeV with the ATLAS detector*, *Phys. Rev. D* **94** (2016) 052002, [[1606.04782](#)].
- [90] ATLAS COLLABORATION collaboration, *Constraint of the Higgs boson self-coupling from Higgs boson differential production and decay measurements*, Tech. Rep. ATL-PHYS-PUB-2019-009, CERN, Geneva, Mar, 2019.
- [91] ATLAS COLLABORATION collaboration, *Constraints on the Higgs boson self-coupling from the combination of single-Higgs and double-Higgs production analyses performed with the ATLAS experiment*, Tech. Rep. ATLAS-CONF-2019-049, CERN, Geneva, Oct, 2019.
- [92] ATLAS COLLABORATION collaboration, *Study of the double Higgs production channel $H(\rightarrow b\bar{b})H(\rightarrow \gamma\gamma)$ with the ATLAS experiment at the HL-LHC*, Tech. Rep. ATL-PHYS-PUB-2017-001, CERN, Geneva, Jan, 2017.
- [93] ATLAS COLLABORATION collaboration, *Measurement prospects of the pair production and self-coupling of the Higgs boson with the ATLAS experiment at the HL-LHC*, Tech. Rep. ATL-PHYS-PUB-2018-053, CERN, Geneva, Dec, 2018.
- [94] J. H. Kim, K. Kong, K. T. Matchev and M. Park, *Probing the Triple Higgs Self-Interaction at the Large Hadron Collider*, *Phys. Rev. Lett.* **122** (2019) 091801, [[1807.11498](#)].

- [95] J. H. Kim, M. Kim, K. Kong, K. T. Matchev and M. Park, *Portraying Double Higgs at the Large Hadron Collider*, *JHEP* **09** (2019) 047, [[1904.08549](#)].
- [96] M. J. Dolan, C. Englert and M. Spannowsky, *Higgs self-coupling measurements at the LHC*, *JHEP* **10** (2012) 112, [[1206.5001](#)].
- [97] A. J. Barr, M. J. Dolan, C. Englert and M. Spannowsky, *Di-Higgs final states augMT2ed – selecting hh events at the high luminosity LHC*, *Phys. Lett. B* **728** (2014) 308–313, [[1309.6318](#)].
- [98] V. Barger, L. L. Everett, C. B. Jackson and G. Shaughnessy, *Higgs-Pair Production and Measurement of the Triscalar Coupling at LHC(8,14)*, *Phys. Lett. B* **728** (2014) 433–436, [[1311.2931](#)].
- [99] F. Kling, T. Plehn and P. Schichtel, *Maximizing the significance in Higgs boson pair analyses*, *Phys. Rev. D* **95** (2017) 035026, [[1607.07441](#)].
- [100] A. Alves, T. Ghosh and K. Sinha, *Can We Discover Double Higgs Production at the LHC?*, *Phys. Rev. D* **96** (2017) 035022, [[1704.07395](#)].
- [101] A. Adhikary, S. Banerjee, R. K. Barman, B. Bhattacharjee and S. Niyogi, *Revisiting the non-resonant Higgs pair production at the HL-LHC*, *JHEP* **07** (2018) 116, [[1712.05346](#)].
- [102] J. Amacker et al., *Higgs self-coupling measurements using deep learning and jet substructure in the $b\bar{b}b\bar{b}$ final state*, [2004.04240](#).
- [103] M. Abdughani, D. Wang, L. Wu, J. M. Yang and J. Zhao, *Probing triple Higgs coupling with machine learning at the LHC*, [2005.11086](#).
- [104] G. Heinrich, S. Jones, M. Kerner, G. Luisoni and L. Scyboz, *Probing the trilinear Higgs boson coupling in di-Higgs production at NLO QCD including parton shower effects*, *JHEP* **06** (2019) 066, [[1903.08137](#)].
- [105] E. Arganda, C. Garcia-Garcia and M. J. Herrero, *Probing the Higgs self-coupling through double Higgs production in vector boson scattering at the LHC*, *Nucl. Phys. B* **945** (2019) 114687, [[1807.09736](#)].
- [106] J. Chang, K. Cheung, J. S. Lee, C.-T. Lu and J. Park, *Higgs-boson-pair production $H(\rightarrow b\bar{b})H(\rightarrow \gamma\gamma)$ from gluon fusion at the HL-LHC and HL-100 TeV hadron collider*, *Phys. Rev. D* **100** (2019) 096001, [[1804.07130](#)].
- [107] D. Asner et al., *ILC Higgs White Paper*, in *Community Summer Study 2013: Snowmass on the Mississippi*, 10, 2013. [1310.0763](#).
- [108] T. Barklow, K. Fujii, S. Jung, M. E. Peskin and J. Tian, *Model-Independent Determination of the Triple Higgs Coupling at e^+e^- Colliders*, *Phys. Rev. D* **97** (2018) 053004, [[1708.09079](#)].
- [109] F. Maltoni, D. Pagani and X. Zhao, *Constraining the Higgs self-couplings at e^+e^- colliders*, *JHEP* **07** (2018) 087, [[1802.07616](#)].
- [110] R. Li, X.-M. Shen, B.-W. Wang, K. Wang and G. Zhu, *Probing the trilinear Higgs boson self-coupling via single Higgs production at the LHeC*, *Phys. Rev. D* **101** (2020) 075036, [[1910.09424](#)].

- [111] M. McCullough, *An Indirect Model-Dependent Probe of the Higgs Self-Coupling*, *Phys. Rev. D* **90** (2014) 015001, [[1312.3322](#)].
- [112] F. Maltoni, D. Pagani, A. Shivaji and X. Zhao, *Trilinear Higgs coupling determination via single-Higgs differential measurements at the LHC*, *Eur. Phys. J. C* **77** (2017) 887, [[1709.08649](#)].
- [113] S. Di Vita, C. Grojean, G. Panico, M. Riembau and T. Vantalon, *A global view on the Higgs self-coupling*, *JHEP* **09** (2017) 069, [[1704.01953](#)].
- [114] W. Bizon, M. Gorbahn, U. Haisch and G. Zanderighi, *Constraints on the trilinear Higgs coupling from vector boson fusion and associated Higgs production at the LHC*, *JHEP* **07** (2017) 083, [[1610.05771](#)].
- [115] G. Degrandi, P. P. Giardino, F. Maltoni and D. Pagani, *Probing the Higgs self coupling via single Higgs production at the LHC*, *JHEP* **12** (2016) 080, [[1607.04251](#)].
- [116] F. Goertz, A. Papaefstathiou, L. L. Yang and J. Zurita, *Higgs Boson self-coupling measurements using ratios of cross sections*, *JHEP* **06** (2013) 016, [[1301.3492](#)].
- [117] G. D. Kribs, A. Maier, H. Rzehak, M. Spannowsky and P. Waite, *Electroweak oblique parameters as a probe of the trilinear Higgs boson self-interaction*, *Phys. Rev. D* **95** (2017) 093004, [[1702.07678](#)].
- [118] M. L. Mangano, G. Ortona and M. Selvaggi, *Measuring the Higgs self-coupling via Higgs-pair production at a 100 TeV p-p collider*, [2004.03505](#).
- [119] S. Banerjee, F. Krauss and M. Spannowsky, *Revisiting the $t\bar{t}hh$ channel at the FCC-hh*, *Phys. Rev. D* **100** (2019) 073012, [[1904.07886](#)].
- [120] S. Banerjee, C. Englert, M. L. Mangano, M. Selvaggi and M. Spannowsky, *$hh + jet$ production at 100 TeV*, *Eur. Phys. J. C* **78** (2018) 322, [[1802.01607](#)].
- [121] W. Bizoń, U. Haisch and L. Rottoli, *Constraints on the quartic Higgs self-coupling from double-Higgs production at future hadron colliders*, *JHEP* **10** (2019) 267, [[1810.04665](#)].
- [122] D. Gonçalves, T. Han, F. Kling, T. Plehn and M. Takeuchi, *Higgs boson pair production at future hadron colliders: From kinematics to dynamics*, *Phys. Rev. D* **97** (2018) 113004, [[1802.04319](#)].
- [123] A. J. Barr, M. J. Dolan, C. Englert, D. E. Ferreira de Lima and M. Spannowsky, *Higgs Self-Coupling Measurements at a 100 TeV Hadron Collider*, *JHEP* **02** (2015) 016, [[1412.7154](#)].
- [124] R. Contino et al., *Physics at a 100 TeV pp collider: Higgs and EW symmetry breaking studies*, *CERN Yellow Rep.* (2017) 255–440, [[1606.09408](#)].
- [125] H.-J. He, J. Ren and W. Yao, *Probing new physics of cubic Higgs boson interaction via Higgs pair production at hadron colliders*, *Phys. Rev. D* **93** (2016) 015003, [[1506.03302](#)].
- [126] T. Corbett, A. Joglekar, H.-L. Li and J.-H. Yu, *Exploring Extended Scalar Sectors with Di-Higgs Signals: A Higgs EFT Perspective*, *JHEP* **05** (2018) 061, [[1705.02551](#)].
- [127] S. Kudy, H. Saygı n, I. Ho,s and F. Çetin, *Projections for Neutral Di-Boson and Di-Higgs Interactions at FCC-he Collider*, *Nucl. Phys. B* **932** (2018) 1–14, [[1702.00185](#)].

- [128] S. Homiller and P. Meade, *Measurement of the Triple Higgs Coupling at a HE-LHC*, *JHEP* **03** (2019) 055, [[1811.02572](#)].
- [129] M. Cepeda et al., *Report from Working Group 2: Higgs Physics at the HL-LHC and HE-LHC*, vol. 7, pp. 221–584. 12, 2019. [1902.00134](#). 10.23731/CYRM-2019-007.221.
- [130] J. Baglio, A. Djouadi, R. Gröber, M. M. Mühlleitner, J. Quevillon and M. Spira, *The measurement of the Higgs self-coupling at the LHC: theoretical status*, *JHEP* **04** (2013) 151, [[1212.5581](#)].
- [131] A. Hoecker, P. Speckmayer, J. Stelzer, J. Therhaag, E. von Toerne, H. Voss et al., *TMVA - Toolkit for Multivariate Data Analysis*, *ArXiv Physics e-prints* (Mar., 2007) , [[physics/0703039](#)].
- [132] T. Chen and C. Guestrin, *Xgboost*, *Proceedings of the 22nd ACM SIGKDD International Conference on Knowledge Discovery and Data Mining* (Aug, 2016) .
- [133] I. Goodfellow, Y. Bengio and A. Courville, *Deep Learning*. MIT Press, 2016.
- [134] <https://www.tensorflow.org/>.
- [135] <https://keras.io/>.
- [136] J. Alwall, R. Frederix, S. Frixione, V. Hirschi, F. Maltoni, O. Mattelaer et al., *The automated computation of tree-level and next-to-leading order differential cross sections, and their matching to parton shower simulations*, *JHEP* **07** (2014) 079, [[1405.0301](#)].
- [137] NNPDF collaboration, R. D. Ball et al., *Parton distributions for the LHC Run II*, *JHEP* **04** (2015) 040, [[1410.8849](#)].
- [138] *ATLAS Run 1 Pythia8 tunes*, Tech. Rep. ATL-PHYS-PUB-2014-021, CERN, Geneva, Nov, 2014.
- [139] T. Sjöstrand, S. Ask, J. R. Christiansen, R. Corke, N. Desai, P. Ilten et al., *An Introduction to PYTHIA 8.2*, *Comput. Phys. Commun.* **191** (2015) 159–177, [[1410.3012](#)].
- [140] DELPHES 3 collaboration, J. de Favereau, C. Delaere, P. Demin, A. Giammanco, V. Lemaître, A. Mertens et al., *DELPHES 3, A modular framework for fast simulation of a generic collider experiment*, *JHEP* **02** (2014) 057, [[1307.6346](#)].
- [141] M. Cacciari, G. P. Salam and G. Soyez, *The Anti- $k(t)$ jet clustering algorithm*, *JHEP* **04** (2008) 063, [[0802.1189](#)].
- [142] M. Cacciari, G. P. Salam and G. Soyez, *FastJet User Manual*, *Eur. Phys. J.* **C72** (2012) 1896, [[1111.6097](#)].
- [143] CMS collaboration, A. M. Sirunyan et al., *Identification of heavy-flavour jets with the CMS detector in pp collisions at 13 TeV*, *JINST* **13** (2018) P05011, [[1712.07158](#)].
- [144] M. L. Mangano, M. Moretti, F. Piccinini and M. Treccani, *Matching matrix elements and shower evolution for top-quark production in hadronic collisions*, *JHEP* **01** (2007) 013, [[hep-ph/0611129](#)].
- [145] J. C. Collins and D. E. Soper, *Angular distribution of dileptons in high-energy hadron collisions*, *Phys. Rev. D* **16** (Oct, 1977) 2219–2225.

- [146] E. Richter-Was and Z. Was, *Separating electroweak and strong interactions in Drell–Yan processes at LHC: leptons angular distributions and reference frames*, *Eur. Phys. J. C* **76** (2016) 473, [[1605.05450](#)].
- [147] <https://twiki.cern.ch/twiki/bin/view/LHCPhysics/LHCHXSWG1HELHCXsecs>.
- [148] <https://twiki.cern.ch/twiki/bin/view/LHCPhysics/LHCHXSWGHH>.
- [149] A. Barr, C. Lester and P. Stephens, *$m(T_2)$: The Truth behind the glamour*, *J. Phys.* **G29** (2003) 2343–2363, [[hep-ph/0304226](#)].
- [150] C. G. Lester and D. J. Summers, *Measuring masses of semiinvisibly decaying particles pair produced at hadron colliders*, *Phys. Lett.* **B463** (1999) 99–103, [[hep-ph/9906349](#)].
- [151] A. Elagin, P. Murat, A. Pranko and A. Safonov, *A New Mass Reconstruction Technique for Resonances Decaying to di-tau*, *Nucl. Instrum. Meth.* **A654** (2011) 481–489, [[1012.4686](#)].
- [152] ATLAS collaboration, *Higgs Pair Production in the $H(\rightarrow \tau\tau)H(\rightarrow b\bar{b})$ channel at the High-Luminosity LHC*, .
- [153] CMS COLLABORATION collaboration, *Performance of reconstruction and identification of tau leptons in their decays to hadrons and tau neutrino in LHC Run-2*, Tech. Rep. CMS-PAS-TAU-16-002, CERN, Geneva, 2016.
- [154] <https://twiki.cern.ch/twiki/bin/view/LHCPhysics/TtbarNNLO>.
- [155] A. Lazopoulos, T. McElmurry, K. Melnikov and F. Petriello, *Next-to-leading order QCD corrections to $t\bar{t}Z$ production at the LHC*, *Phys. Lett.* **B666** (2008) 62–65, [[0804.2220](#)].
- [156] M. L. Graesser and J. Shelton, *Hunting Mixed Top Squark Decays*, *Phys. Rev. Lett.* **111** (2013) 121802, [[1212.4495](#)].
- [157] P. Konar, K. Kong and K. T. Matchev, *\sqrt{s}_{min} : A global inclusive variable for determining the mass scale of new physics in events with missing energy at hadron colliders*, *JHEP* **03** (2009) 085, [[0812.1042](#)].
- [158] <https://cp3.irmp.ucl.ac.be/projects/madgraph/wiki/HiggsPairProduction>.
- [159] P. Agrawal, D. Saha, L.-X. Xu, J.-H. Yu and C. Yuan, *Determining the shape of the Higgs potential at future colliders*, *Phys. Rev. D* **101** (2020) 075023, [[1907.02078](#)].

A Outlining the generation cuts and production cross sections for the signal and backgrounds

Process	Signal and Backgrounds	Generation-level cuts ($\ell = e^\pm, \mu^\pm$) (NA : Not Applied)	Cross section (fb)
$b\bar{b}\gamma\gamma$	Signal ($hh \rightarrow b\bar{b}\gamma\gamma$)	NA	0.37
	$b\bar{b}\gamma\gamma + \text{jet}$	$p_{T,j/b/\gamma} > 20 \text{ GeV}$, $ \eta_{j/b/\gamma} < 5.0$, $\Delta R_{j,b,\gamma}^5 > 0.2$, $m_{bb} > 50 \text{ GeV}$, $110 < m_{\gamma\gamma} < 140 \text{ GeV}$	134.84
	$c\bar{c}\gamma\gamma$	$p_{T,j/\gamma} > 20 \text{ GeV}$, $ \eta_{j/\gamma} < 5.0$, $\Delta R_{j,\gamma} > 0.2$, $m_{jj} > 50 \text{ GeV}$, $110 < m_{\gamma\gamma} < 140 \text{ GeV}$	705.02 ⁶
	$j\bar{j}\gamma\gamma$	same as $c\bar{c}\gamma\gamma$	12772.97 ⁷
	$t\bar{t}h$, $h \rightarrow \gamma\gamma$	$p_{T,b/\gamma} > 20 \text{ GeV}$, $ \eta_{b/\gamma} < 5.0$, $\Delta R_{bb/\gamma\gamma} > 0.2$	5.19
	$b\bar{b}h$, $h \rightarrow \gamma\gamma$	$p_{T,b/\gamma} > 20 \text{ GeV}$, $ \eta_{b/\gamma} < 5.0$, $\Delta R_{b,\gamma} > 0.2$, $m_{bb} > 50 \text{ GeV}$	0.32
	Zh , $Z \rightarrow b\bar{b}$, $h \rightarrow \gamma\gamma$	same as $b\bar{b}h$	0.46
	$b\bar{b}j\bar{j}$	$p_{T,j/b} > 20 \text{ GeV}$, $ \eta_{j/b} < 5.0$, $\Delta R_{j,b} > 0.2$, $m_{bb} > 50 \text{ GeV}$, $m_{jj} > 50 \text{ GeV}$	650847671.98 ⁸
	$b\bar{b}j\gamma$	$p_{T,j/b/\gamma} > 20 \text{ GeV}$, $ \eta_{j/b/\gamma} < 5.0$, $\Delta R_{j,b,\gamma} > 0.2$, $m_{bb} > 50 \text{ GeV}$	1078323.46 ⁸
	$c\bar{c}j\gamma$	$p_{T,b/\gamma} > 20 \text{ GeV}$, $ \eta_{b/\gamma} < 5.0$, $\Delta R_{bb/\gamma\gamma} > 0.2$	4399502.87 ⁶⁸
	$Z\gamma\gamma + \text{jet}$, $Z \rightarrow b\bar{b}$	same as $b\bar{b}\gamma\gamma + \text{jet}$	3.56
	$hc\bar{c}$, $h \rightarrow \gamma\gamma$	$p_{T,j/\gamma} > 20 \text{ GeV}$, $ \eta_{j/\gamma} < 5.0$, $\Delta R_{j,\gamma} > 0.2$, $m_{jj} > 50 \text{ GeV}$	0.14 ⁶
	$hj\bar{j}$, $h \rightarrow \gamma\gamma$	same as $hc\bar{c}$	20.19 ⁷
$b\bar{b}\tau\tau$	Signal ($hh \rightarrow b\bar{b}\tau\tau$)	NA	10.22
	$t\bar{t}$ had	$p_{T,j/b} > 20 \text{ GeV}$, $ \eta_{j/b} < 5.0$, $\Delta R_{j,b} > 0.2$, $m_{bb} > 50 \text{ GeV}$	657474.63 ⁹
	$t\bar{t}$ semi-lep	$p_{T,j/b} > 20 \text{ GeV}$, $p_{T,\ell} > 15 \text{ GeV}$, $ \eta_{j/b/\ell} < 5.0$, $\Delta R_{j,b,\ell} > 0.2$, $m_{bb} > 50 \text{ GeV}$	803269.61
	$t\bar{t}$ lep	same as $t\bar{t}$ semi-lep	245010.26
	$b\bar{b}\tau\tau$	$p_{T,b} > 20 \text{ GeV}$, $p_{T,\ell} > 15 \text{ GeV}$, $ \eta_{b/\ell} < 5.0$, $\Delta R_{b,\ell} > 0.2$, $m_{bb} > 50 \text{ GeV}$, $m_{\ell\ell} > 30 \text{ GeV}$	8280.06
	$b\bar{b}h$, $h \rightarrow \tau\tau$	$p_{T,b} > 20 \text{ GeV}$, $p_{T,\ell} > 15 \text{ GeV}$, $ \eta_{b/\ell} < 5.0$, $\Delta R_{b,\ell} > 0.2$, $m_{bb} > 50 \text{ GeV}$	6.14
	Zh	NA	56.39
	$t\bar{t}h$	NA	2860.00
	$t\bar{t}Z$	NA	3477.02
	$t\bar{t}W$	NA	986.58
	$bbj\bar{j}$	$p_{T,j/b} > 20 \text{ GeV}$, $ \eta_{j/b} < 5.0$, $\Delta R_{j,b} > 0.2$, $m_{bb} > 50 \text{ GeV}$, $m_{jj} > 50 \text{ GeV}$	650847671.98 ⁹

Table 11: Generation level cuts and cross-sections for the various backgrounds used in the analyses.

⁵ $\Delta R_{b,j,\gamma}$ means ΔR between all possible combination of $b/j/\gamma$.

⁶ $c \rightarrow b$ average fake rate is 3.5%^[143].

⁷ $j \rightarrow b$ average fake rate is 0.135%^[143].

⁸ $j \rightarrow \gamma$ fake rate is 0.05%^[92].

⁹ $j \rightarrow \tau$ fake rate is 0.35%^[153].

Process	Backgrounds	Generation-level cuts ($\ell = e^\pm, \mu^\pm$) (NA : Not Applied)	Cross section (fb)
$b\bar{b}WW^*$	Signal ($hh \rightarrow b\bar{b}WW^*, W \rightarrow \ell\nu$)	NA	34.82
	$t\bar{t}$ lep	$p_{T,j/b} > 20$ GeV, $p_{T,\ell} > 15$ GeV, $ \eta_{j/b/\ell} < 5.0$, $\Delta R_{j,b,\ell} > 0.2$, $m_{bb} > 50$ GeV	245010.26
	$\ell\ell b\bar{b}$	$p_{T,b} > 20$ GeV, $p_{T,\ell} > 15$ GeV, $ \eta_{b/\ell} < 5.0$, $\Delta R_{b,\ell} > 0.2$, $m_{bb} > 50$ GeV	25794.58
	$t\bar{t}h$	NA	2860.00
	$t\bar{t}Z$	NA	3477.02
	$t\bar{t}W$	NA	986.58
	tW	$p_{T,j/b} > 20$ GeV, $p_{T,\ell} > 10$ GeV, $ \eta_{j/b/\ell} < 5.0$, $\Delta R_{j,b,\ell} > 0.2$, $m_{bb} > 50$ GeV	6.59
$WW^*\gamma\gamma$	Signal ($hh \rightarrow WW^*\gamma\gamma, W \rightarrow \ell\nu$)	NA	0.14
	$t\bar{t}h, h \rightarrow \gamma\gamma, t \rightarrow bW \rightarrow b\ell\nu$	$p_{T,\gamma} > 20$ GeV, $p_{T,\ell} > 10$ GeV, $ \eta_{\gamma/\ell} < 5.0$, $\Delta R_{\gamma\gamma/\ell\ell} > 0.2$	1.74
	Zh + jets, $Z \rightarrow \ell\ell, h \rightarrow \gamma\gamma$	$p_{T,j/\gamma} > 20$ GeV, $p_{T,\ell} > 10$ GeV, $ \eta_{j/\gamma/\ell} < 5.0$, $\Delta R_{\gamma\gamma/\ell\ell} > 0.2$	0.29
	$\ell\ell\gamma\gamma$ + jet	$p_{T,j/\gamma} > 20$ GeV, $p_{T,\ell} > 10$ GeV, $ \eta_{j/\gamma/\ell} < 5.0$, $m_{\ell\ell} > 20$ GeV, $\Delta R_{\gamma\gamma/\ell\ell/\gamma\ell/\gamma j} > 0.2$, $120 < m_{\gamma\gamma} < 130$ GeV	3.77
$b\bar{b}ZZ^*$	Signal ($hh \rightarrow b\bar{b}ZZ^*, Z \rightarrow \ell\ell$)	NA	0.0218
	$t\bar{t}h$ (all categories combined)	$p_{T,b} > 20$ GeV, $ \eta_b < 5.0$, $\Delta R_{bb} > 0.2$, $m_{bb} > 50$ GeV	171.47
	$t\bar{t}Z, (t \rightarrow bW, W \rightarrow \ell\nu), (Z \rightarrow \ell\ell)$		36.92
	$Zh, Z \rightarrow b\bar{b}, h \rightarrow ZZ^* \rightarrow 4\ell$		0.06
	$Wh, W \rightarrow cs, h \rightarrow ZZ^* \rightarrow 4\ell$		0.21 ⁶⁷
	$Whc, W \rightarrow cs, h \rightarrow ZZ^* \rightarrow 4\ell$		0.003 ⁶
	$ggF\text{-}hbb, h \rightarrow ZZ^* \rightarrow 4\ell$		0.04
	$ggF\text{-}hc\bar{c}, h \rightarrow ZZ^* \rightarrow 4\ell$		0.02 ⁶
	$VBF\text{-}hjj, h \rightarrow ZZ^* \rightarrow 4\ell$		⁷ 0.44×10^{-5}
	Signal ($hh \rightarrow b\bar{b}\mu\mu$)	NA	0.0355
	$t\bar{t}, t \rightarrow bW, W \rightarrow \mu\nu_\mu$	$p_{T,b/\ell} > 20$ GeV, $ \eta_{b/\ell} < 5.0$, $\Delta R_{b,\ell} > 0.2$ $m_{bb} > 50$ GeV, $m_{\ell\ell} > 100$ GeV	12952.01
$b\bar{b}\mu\mu$	$b\bar{b}\mu\mu$	same as $t\bar{t}$	351.28
	$c\bar{c}\mu\mu$		313.79 ⁶
	$j\bar{j}\mu\mu$		13930.93 ⁷
	$Zh, Z \rightarrow b\bar{b}, h \rightarrow \mu\mu$		0.04
	$b\bar{b}h, h \rightarrow \mu\mu$		0.02
	$t\bar{t}h, h \rightarrow \mu\mu$		0.46

Table 12: Generation level cuts and cross-sections for the various backgrounds used in the analyses.